

1 Making Aircraft Vortices Visible to Radar by Spraying Water into the Wake

2 Karim Shariff*

3 *NASA Ames, Moffett Field, California, 94035*

4 **Corresponding author address: NASA Ames, Moffett Field, California, 94035*

5 E-mail: Karim.Shariff@nasa.gov

ABSTRACT

Aircraft trailing vortices pose a danger to following aircraft during take-off and landing. This necessitates spacing rules, based on aircraft type, to be enforced during approach in IFR (Instrument Flight Regulations) conditions; this can limit airport capacity. To help choose aircraft spacing based on the actual location and strength of the wake, it is proposed that wake vortices can be detected using conventional precipitation and cloud radars. This is enabled by spraying a small quantity water into the wake from near the wing. The vortex strength is revealed by the doppler velocity of the droplets. In the present work, droplet size distributions produced by nozzles used for aerial spraying are considered. Droplet trajectory and evaporation in the flow-field is numerically calculated for a heavy aircraft, followed by an evaluation of radar reflectivity at 6 nautical miles behind the aircraft. Small droplets evaporate away while larger droplets fall out of the wake. In the humid conditions that typically prevail during IFR, a sufficient number of droplets remain in the wake and give good signal-to-noise ratios (SNR). For conditions of average humidity, higher frequency radars combined with spectral processing gives good SNR.

23 1. Introduction

24 *a. Motivation*

25 Aircraft trailing vortices are a hazard to following airplanes during take-off and landing (e.g.,
26 Barbagallo 2014). For a review of their dynamics, see Spalart (1998). Due to their mutually
27 induced velocity, a pair of trailing vortices generally descends from the altitude where it was
28 generated. (For exceptions to this in strongly stratified conditions, see Spalart, 1996). Therefore,
29 a wake encounter may occur when a following aircraft finds itself below¹ the path of the leading
30 aircraft. The possibility for this is increased during take-off and landing, and the present work
31 addresses the latter situation. When cleared for a visual approach to landing, the pilot of the
32 following aircraft can visually attempt to remain above the path of the leader by, for example,
33 flying at a higher glide slope to the same touchdown point as the leader. Even in visual approaches,
34 however, things can and do go awry (Barbagallo 2014, §2.3). This means that efforts to find an
35 all-weather wake sensor should be continued.

36 When the ceiling is less than 1000 ft and the visibility less than 3 statute miles, operations
37 must be conducted under Instrument Flight Regulations (IFR). In this case, air traffic controllers
38 maintain separations according to the weight categories of the leading and following aircraft; see
39 Table 1. These separations have started to limit capacity at some airports (Crouch et al. 2001b)
40 and we refer the reader to a report (Broderick et al. 2008) by a committee of the National Research
41 Council entitled “Wake Turbulence: An Obstacle to Increased Air Traffic Capacity.” About two
42 decades ago, NASA initiated the AVOSS (Aircraft Vortex Spacing System) program whose aim
43 was to make aircraft spacing dynamic through a combination of vortex sensing and real-time
44 flowfield simulation. The present work is motivated by the vortex detection aspect of the AVOSS

¹A former colleague, Dr. Vernon Rossow, has long suggested that with GPS and fly-by-wire, the simplest approach to wake avoidance would be for a following aircraft to remain at or above the path of the leader.

45 program. A current effort that has similar aims as the defunct AVOSS program is WakeNet-
46 Europe (www.wakenet.eu). Finally, we mention the development of a system to hasten the break-
47 up of trailing vortices by exciting vortex instabilities through periodic motion of control surfaces
48 (Crouch et al. 2001a,b). Such a system could be implemented together with one for wake detection.

49 *b. Previous work using radar to detect aircraft wakes*

50 The main vortex detection technology tested by the AVOSS program was infrared lidar. A
51 concern raised about lidar was that since water vapor strongly absorbs infrared, it would not be
52 usable in IFR conditions. Another concern is that optical systems are more expensive and difficult
53 to maintain than radar. These concerns motivate consideration of radar.

54 1) CLEAR AIR REFLECTIVITY

55 The first observational and theoretical efforts on radar detection of wakes were in the context
56 of *clear air*. Systematic tests by Gilson (1992) showed that the wake of a C-5A aircraft could
57 be detected by radars having 2–7 MW of peak power at frequencies from 0.162 to 5.67 GHz,
58 with no return at 35 GHz. Shariff and Wray (2002) analyzed the reflectivity in Gilson’s test
59 using a model of a vortex pair descending in a stratified atmosphere, carrying with it an oval of
60 atmospheric air from the altitude at which the wake formed. This leads to a gradient in refractive
61 index between the oval and ambient air. Another mechanism investigated by Shariff and Wray
62 (2002), which has peak reflectivity at a low frequency of 50 MHz, is the pressure (hence density)
63 gradient in each vortex. Both of these mechanisms have some drawbacks for practical use: (a) the
64 radar cross-section is small (-60 to -80 dB m²); (b) the first mechanism depends on atmospheric
65 stratification, which has seasonal, geographic, and diurnal variations; and (c) the frequency of
66 the second mechanism is the same as that of Stratospheric-Tropospheric radars, which have an

67 antenna array on the ground looking upward. For the present application, technology would have
68 to be developed for aiming the radar by use of phasing. Li et al. (2011) extended the work of
69 Shariff and Wray (2002) with a better calculation of the compressibility-induced variation in air
70 density in the wake. More importantly, they showed that the atmospheric gradient of water vapor
71 is wound up into a spiral by each vortex, which allows scattering at high frequencies.

72 Babaresco et al. (2008) conducted tests using an X-band (9.6 GHz) radar for aircraft taking-off
73 and flying straight and level at 1500 m altitude. For the take-off case, the range was about 700 m
74 looking roughly sideways using peak pulse power of only 20 W. For the aircraft at an altitude of
75 1500 m, the radar was looking straight up and the peak pulse power was 75 W. A time doppler plot
76 indicated a spiral structure in each vortex. However, in staring mode, a return is obtained for only
77 five seconds, at most. Babaresco et al. (2008) did not report how far downstream of the aircraft
78 the wake could be detected; it appears that this distance is very short.

79 In conclusion, clear air reflectivity is an interesting prospect, but more careful and better docu-
80 mented observational campaigns combined with theoretical efforts are needed.

81 2) EXPLOITING NATURAL PRECIPITATION

82 A different approach, which the author first heard about from Robert Neece (NASA Langley,
83 personal communication) around 2000, exploits the fact that water droplets (in the form of fog
84 or rain) are present in IFR weather conditions. They are strong radar reflectors, and, when an
85 airplane wake sets these particles into motion, they can be separated from ambient droplets via
86 their doppler signature. This strategy has the advantage that standard doppler weather radars
87 could be used. Seliga and Mead (2009) demonstrated the feasibility of the approach using a W-
88 band (94 GHz) radar in an opportunistic test with only 100 mW of peak power. An analysis of the
89 reflectivity of this mechanism has been conducted by Liu et al. (2013), and further measurements

90 are reported in Babaresco (2012). The main drawback of this approach is that there may be long
91 stretches along the flight path where a sufficient number of natural droplets is unavailable.

92 *c. Present approach*

93 The approach proposed here is related to the use of natural precipitation for wake detection
94 discussed in the previous paragraph, except that, to provide a persistent radar target, water spray
95 is injected into the wake. We envision one nozzle on each side of the airplane that injects the
96 water spray near the wing trailing edge at a specified spanwise location. One possibility for nozzle
97 placement is the aft tip of a flap track fairing. A pump and water tank could be located nearby
98 within the wing.

99 The main constraint imposed by nature is droplet retention in the wake: a nozzle produces
100 a distribution of droplet sizes; the smallest ones evaporate away while the largest ones fall out
101 of the wake due to gravity. However, IFR conditions are correlated with high humidity (§2l).
102 This reduces the rate of evaporation and makes the approach feasible. In a non-IFR case we
103 consider that has moderate humidity, only the Ka and W band radars give sufficient reflectivity in
104 a patch above each vortex. However, it is shown that spectral processing reduces noise and allows
105 detection even when the signal to noise ratio in individual pulse returns is < 1 . Finally, there is
106 no reason why the present approach and that of using natural precipitation could not be combined
107 using the same radar.

108 **2. Calculation methods**

109 *a. General procedure*

110 We use aircraft centered coordinates (x, y, z) , where x is streamwise, y is spanwise, and z is
111 vertical. Air and water are denoted by subscripts ‘a’ and ‘w’, respectively.

112 The calculation has three steps. The first creates a sample of droplet radii $a(t)$ from a size dis-
113 tribution pertinent to aerial spray nozzles. The second step generates a spray trail on the starboard
114 side of the aircraft wake. This involves injecting droplets from the sample into the wake, tracking
115 the position $\mathbf{X}(t)$ of each droplet and its radius $a(t)$ as it evaporates. The flow-field model consists
116 of two counter-rotating vortices whose height decreases with downstream distance x behind the
117 aircraft. The third and final step mirrors the starboard trail to the port side and, for a given set of
118 radar parameters, computes the reflectivity of both trails together.

119 Since it is prohibitive to track all of the actual droplets, the spray trail computed in step two
120 consists of a certain number, N_{comp} , of computational droplets. In the reflectivity calculation, each
121 computational droplet is taken to represent a multiplicity, M_{true} , of actual droplets, which is simply
122 the ratio of the desired injected volume to the volume injected in the computation.

123 The equations for droplet motion and evaporation are integrated using the routine LSODE which
124 is described in Radhakrishnan and Hindmarsh (1993) and available from NETLIB. The routine
125 chooses a time step based on a specified error tolerance. Since the flow-field model we have
126 adopted is steady in a reference frame moving with the aircraft, it is not necessary to inject droplets
127 at every time step, which would continuously increase the number of computational droplets. In-
128 stead, droplets are injected only during a certain time interval Δt_0 at the beginning of the calcula-
129 tion. This set of droplets is then evolved for successive Δt_0 intervals and appended to a file at the
130 end of every Δt_0 interval. At the end of the computation, the file contains a spray trail that is 7 nm
131 miles long, whose radar reflectivity we subsequently analyze. In actual practice, an aircraft would
132 likely not generate a trail of several nautical miles behind it. Rather, it would release the spray for
133 a short period at pre-selected locations during its approach.

134 A detailed description of each part of the procedure is described in the following subsections.
135 The evaporation calculation is described in Appendix A2. To avoid stiffness of the system of evo-

lution equations, droplets are removed from the calculation when their radius becomes $< 20 \mu\text{m}$; at this point their reflectivity is too small to significantly affect the received power.

b. Droplet trajectory

The position $\mathbf{X}(t)$ and velocity $\mathbf{U}(t)$ of a droplet of mass m_d evolves according to

$$\frac{d\mathbf{X}}{dt} = \mathbf{U}(t), \quad (1)$$

$$\frac{d\mathbf{U}}{dt} = \mathbf{F}_D/m_d - g_{\text{eff}}\hat{Z}, \quad (2)$$

where $g_{\text{eff}} = (1 - \rho_a/\rho_w)g$ is the effective gravity accounting for buoyancy. The drag force \mathbf{F}_D is given by

$$\mathbf{F}_D = C_D \frac{1}{2} \rho_a |\mathbf{u}_{\text{rel}}|^2 \pi a^2 \frac{\mathbf{u}_{\text{rel}}}{|\mathbf{u}_{\text{rel}}|}, \quad (3)$$

where

$$\mathbf{u}_{\text{rel}} = \mathbf{u}(\mathbf{X}) - \mathbf{U}, \quad (4)$$

is the velocity of the air flow, $\mathbf{u}(\mathbf{X})$, relative to the droplet. Evaluation of the drag coefficient, C_D , is described in Appendix A1.

c. Droplet size distribution of aerial spray nozzles

When the water jet issues from the nozzle, it will encounter a blast of free-stream air with a speed of 77.2 m s^{-1} . A comparable situation in the literature is that of a cylindrical liquid jet surrounded by an annulus of co-flowing air (Lorenzetto and Lefebvre 1977; Varga et al. 2003) which shows that much smaller droplets are produced than for the case of still air (with the same velocity of the liquid jet). This is due to the occurrence of both the Kelvin-Helmholtz instability and Rayleigh-Taylor instabilities. The former is driven by the shear between the air and liquid flow and leads to a smaller instability wavelength. The latter arises due to the acceleration of liquid droplets by

the drag force of the air stream. If the droplets are too small, they quickly evaporate. To produce larger droplets, both instabilities can be mitigated by reducing the relative velocity between the liquid jet and free-stream air. This is accomplished by increasing the driving pressure. However, if the droplets are too large, they fall out of the wake. Hence, there is an optimum droplet size.

We were fortunate that an experimental study (Fritz and Hoffmann 2015), which uses a wind-tunnel to mimic the free stream air flow, has recently been performed to characterize the droplet size distribution produced by nozzles used for aerial agricultural spraying. This study did indeed show that larger pressures produce larger droplets. Dr. B. Fritz kindly provided us with an Excel program, developed from that study, which gives parameters of the droplet size distribution for various nozzles, free-stream speeds, and driving pressures. Use of these parameters is now described.

Let $p(a)$ be the probability density such that $p(a)da$ is the probability that the droplet radius is in the interval $[a, a + da]$. The log-normal distribution

$$p(a) = \frac{1}{\sqrt{2\pi}a\sigma} e^{-\ln^2(a/a_0)/2\sigma^2}, \quad (5)$$

with parameters a_0 and σ , is commonly used in the spray literature. Fritz's Excel program provides information about the function $Q(a)$, defined to be the fractional volume occupied by droplets of radius $\leq a$. One can show from appropriately integrating (5) that

$$Q(a) = \frac{1}{2} (1 + \operatorname{erf} \xi), \quad (6)$$

where

$$\xi \equiv \frac{1}{\sqrt{2}\sigma} [\ln(a/a_0) - 3\sigma^2]. \quad (7)$$

The Excel program provides $a_{0.5}$ and $a_{0.9}$ defined such that $Q(a_{0.5}) = 0.5$ and $Q(a_{0.9}) = 0.9$. Using them, (6) can be numerically inverted to yield the parameters a_0 and σ of the log-normal

172 distribution (5). The Excel program also provides $a_{0,1}$, which we did not use because we wished
 173 to nail the size distribution for large droplets which contribute most to reflectivity.

174 *d. Choice of nozzle*

175 What is the best drop size distribution? A set of N_d droplets over which the incident beam is
 176 assumed to have uniform intensity, has a reflectivity proportional to (e.g., Doviak and Zrnić 1984,
 177 p. 58)

$$\zeta = \sum_{i=1}^{N_d} a_i^6, \quad (8)$$

178 assuming Rayleigh scattering. Maximizing this subject to fixed volume of water and fixed N_d gives
 179 the result that all droplets must be of the same size. Given this result, maximizing ζ with respect
 180 to the number N_d subject to fixed volume gives $N_d = 1$, i.e., all the volume must be in one droplet.
 181 However, such a droplet would likely fall too rapidly. To minimize droplet loss by sedimentation,
 182 droplets must not have a terminal velocity larger than the vortex descent speed, $W_{\text{descent}} = 1.75$
 183 m s^{-1} in the present case. Consulting the terminal velocity plot in Pruppacher and Klett (1997,
 184 p. 416) we conclude that a must be $\leq 200 \mu\text{m}$. Hence the best distribution is uniform with a drop
 185 radius $a = 200 \mu\text{m}$. Since the rate of droplet evaporation is $\propto 1/a$, i.e., small droplets evaporate
 186 faster than larger ones, the above conclusion is not altered by including evaporation.

187 The above considerations suggest that the following “rate of ζ ” could be used to initially evaluate
 188 different nozzles without having to perform an evaporation and reflectivity calculation:

$$\dot{\zeta}_{\text{nozzle}}^{<} \equiv \frac{1}{\Delta t} \sum_{i: a_i < 200 \mu\text{m}}^{N_d(\Delta t)} a_i^6, \quad (9)$$

189 where the $<$ superscript denotes the exclusion from the sum of droplets that fall away and $N_d(\Delta t)$
 190 denotes the number of droplets produced by the nozzle in a period Δt . This suggestion will be
 191 tested in §3h.

Table 2 lists the parameters for four candidate nozzles and operating conditions that were selected from B. Fritz’s Excel program based on having peak probability density at a large radius (which rarely exceeded $100\ \mu\text{m}$) and a high flow-rate. The flow-rate for nozzle 1 was provided by Calvin Kroes (private communication) of CP Products. For nozzles 2 and 3, flow-rates were extrapolated from the values of 5.30 gpm and 2.45 gpm, respectively, at 60 psi reported on the manufacturer’s data sheets (www.translandllc.com/wp-content/uploads/2015/08/Aerial-Flow-Chart-20152.pdf and www.cpproductsinc.com/images/stories/downloads/Misc-Tables/A1-Web%20Aerial%20Tip%20Rate%20Chart.pdf). The extrapolations assumed a square-root dependence of flow-rate on pressure (Lefebvre 1989, p. 157) expected from Bernoulli’s principle, and which the manufacturer’s data follows well. For nozzle 4, the flow-rate versus pressure provided on the manufacturer’s website has a linear rather than square-root dependence. We are grateful to Dr. Brad Fritz (USDA) for measuring the actual flow-rate for us. It turned out to be much lower than the value provided by on the website.

e. Droplet injection in the computation

Let the origin of coordinates be in the symmetry plane of the aircraft (which corresponds to $y = 0$) with same axial and vertical location as the droplet injector. Droplets are injected in a grid pattern within a square of width w_{square} in the yz -plane. The pattern consists of $n_{\text{square}} \times n_{\text{square}}$ droplets. The square is centered at $(x, y, z) = (0, fb/2, 0)$, where f represents the fractional spanwise distance from the aircraft center plane to the wing-tip, and was chosen to be $f = 0.5$. A square shape was chosen because the nozzles we have selected are not of the flat fan type. The streamwise extent of the computed mist trail was chosen to be $\ell_{\text{trail}} = 7\ \text{nm}$ (168 seconds of elapsed time from injection) since we wish to detect the trail at 6 nm, the longest distance for which one would want to detect the wake of a heavy aircraft under current separation rules; see Table 1.

215 The square pattern is injected n_x times and the time interval between injections is Δt_{inject} , whose
 216 value is chosen so that the x spacing between droplets is the same as in the cross-sectional (yz)
 217 plane. After a time period $\Delta t_0 \equiv n_x \Delta t_{\text{inject}}$, an $n_{\text{square}}^2 \times n_x$ slab of particles has been injected, which
 218 is then advanced for successive Δt_0 periods to form the entire trail. Inertial particles with a small
 219 Stokes number tend to an attractor (Haller and Sapsis 2008; Sapsis and Haller 2010) independent
 220 of injection location, and therefore where droplets end-up should be insensitive to where they are
 221 injected. A brief check on insensitivity to initial conditions will be presented in §3b.

222 The initial velocity of droplets is set equal to the air velocity, which is justified as follows. From
 223 the equations of droplet motion, (2)–(4), the characteristic relaxation time for a droplet to start
 224 following a new air speed, imposed at $t = 0$, say, is

$$\tau_{\text{relax}} \equiv \left| \frac{1}{u_{\text{rel}}} \frac{du_{\text{rel}}}{dt} \right|_0^{-1} = \frac{16}{3} \frac{\rho_w}{\rho_a} \frac{a^2}{v_a} (\text{Re } C_D)_0^{-1}. \quad (10)$$

225 where the subscript ‘0’ means that the quantity is calculated at $t = 0$. From this, the characteristic
 226 relaxation distance, $\ell_{\text{relax}} = u_{\text{rel}}(0) \tau_{\text{relax}}$ can be evaluated. Note that the initial air speed relative to
 227 the water jet is given by $u_{\text{rel}}(0) = U_{\text{app}} - U_{\text{exit}}$, where U_{app} is the approach velocity of the aircraft
 228 given in Table 3, and U_{exit} is the exit velocity of the water jet given in Table 2. The experiment of
 229 Fritz and Hoffmann (2015) measured the size distribution 1.8 m downstream of the nozzle for all
 230 straight-stream nozzles. This value is from a private communication from B. Fritz and represents
 231 a correction from a value of 1.5 m reported in Fritz and Hoffmann (2015). Figure 1b plots ℓ_{relax} as
 232 a function of drop radius for nozzle 1. Inspecting it together with the size distribution in Figure 1a,
 233 we conclude that most of the droplets are following the air stream at the measurement station of
 234 the experiment. If this had not been the case and there had been a relative velocity large enough
 235 to give Weber numbers $\gtrsim 10$, then it would have been necessary to model further droplet break-up
 236 using a secondary break-up model (e.g., Apte et al. 2003).

237 *f. Flowfield of two counter-rotating wing-tip vortices*

238 We consider an aircraft flying straight and level at altitude $z_0 = 0$ in aircraft coordinates. The
 239 velocity field of the airflow in the wake is denoted by lower case $\mathbf{u}(\mathbf{x})$. This velocity field consists
 240 of the free stream, $U_{\text{app}}\hat{\mathbf{x}}$ (where U_{app} is the approach speed of the aircraft), superposed with the
 241 flow induced by a pair of counter-rotating vortices with circulations $\pm\Gamma$. The centerline of each
 242 vortex is at spanwise location $y_{\text{vort}} = \pm b_0$. Due to their mutually induced velocity, the height
 243 $z_{\text{vort}}(x)$ of the vortex pair decreases with distance x behind the wing as follows:

$$z_{\text{vort}}(x) = z_0 - W_{\text{desc}}t, \quad (11)$$

244 where $W_{\text{desc}} = \Gamma/2\pi b_0$ is the descent speed of the vortex pair. The quantity $t = x/U_{\text{app}}$ is time
 245 since the vortex at x was shed from the wing.

246 Each vortex induces a circumferential velocity $u_\theta(r)$ in the cross-plane (yz). For $u_\theta(r)$, a profile
 247 fit to flight data by P. Spalart (Private communication) of Boeing is used:

$$u_\theta = \frac{\Gamma}{2\pi r} \begin{cases} 1188.59\eta^2, & \eta < 0.0103; \\ \left[1 + (1.27 + 0.25 \log \eta)^{-14}\right]^{-1/14}, & \text{otherwise;} \end{cases} \quad (12)$$

248 where $\eta \equiv r/b_0$.

249 For an elliptically loaded wing, lifting line theory (Batchelor 1967) gives the vortex spacing as

$$b_0 = \frac{\pi}{4}b, \quad (13)$$

250 where b is the wingspan, and the vortex circulation as

$$\Gamma = \frac{W}{\rho_a U_{\text{app}} b_0}, \quad (14)$$

251 where W is the aircraft weight. We use the parameters for a typical heavy aircraft given in Table 3.

252 *g. Calculation of the received signal and power*

253 A pulse-doppler radar transmits a train of square wave pulses that modulate a carrier wave
 254 of frequency $f = 2\pi/\omega$. The duration of each pulse is τ and the pulse repetition frequency is
 255 f_{PRF} . After each pulse is transmitted, the transmit-receive switch is set to the receive position
 256 and the incoming signal is sampled. Each sample at time t is said to come from the *range gate*
 257 $r = c(t - t_t)/2$, where t_t is the transmit time of the pulse and the factor of two accounts for the
 258 round-trip. Throughout, we consider the case where the transmitting and receiving antenna are the
 259 same, the so-called mono-static case.

260 1) RESOLUTION SHELL

261 An important concept is that of the *resolution volume*, $\mathcal{R}_\tau(t)$, at time t , associated with a single
 262 pulse of finite duration, τ (e.g., Yuter 2003, p. 1836). It is defined as the volume from which a
 263 signal is received *at a fixed time* t due to scattering by the pulse. Let t_t mark the beginning of the
 264 pulse at the transmitter. A signal from a scatterer at distance r will be received in the time interval

$$t - t_t = 2r/c + \xi \tau, \quad 0 \leq \xi \leq 1, \quad (15)$$

265 where $\xi = 0$ corresponds to leading edge of the pulse and $\xi = 1$ to its trailing edge. Solving (15)
 266 for r gives

$$r = c(t - t_t - \xi \tau)/2, \quad 0 \leq \xi \leq 1. \quad (16)$$

267 Equation (16) defines a spherical shell (called the resolution volume) from which a signal is re-
 268 ceived at the fixed time t . The next subsection describes how the complex voltage received at
 269 a given time is evaluated by summing the complex voltages from each droplet in the resolution
 270 volume.

271 2) RECEIVED POWER AND SIGNAL-TO-NOISE RATIO

272 The material in this subsection is adapted from the texts Doviak and Zrnić (1984) and Ishimaru
 273 (1978). Let the “voltage” of the transmitted pulse be (the real part of)

$$V_t(t) = \begin{cases} V_0 e^{i\omega t}, & t \leq \tau; \\ 0, & \text{otherwise;} \end{cases} \quad (17)$$

274 where V_0 is a complex amplitude, τ is the pulse width, and “voltage” is defined such that the
 275 instantaneous transmitted power is $P_t(t) = V_t(t)V_t^*(t)$. The voltage at the input terminals of the
 276 receiver is (the real part of) the following summation over droplets:

$$V(t) = \sum_{m=1}^{N_d} A_m(t) e^{i\omega_m(t-2r_m/c)}, \quad (18)$$

277 where A_m is a complex scattering amplitude and

$$\omega_m \equiv \omega(1 - 2u_m/c) \quad (19)$$

278 is the twice doppler-shifted frequency (u_m being the radial velocity of the m th droplet) and r_m is
 279 the distance to each droplet. The summation in (18) is taken over the N_d droplets in the resolution
 280 volume associated with the pulse.

281 The complex scattering amplitude due to each droplet is

$$A_m = \left[\frac{\lambda^2 \ell_w \ell_B}{(4\pi)^3} \frac{G^2(\theta_m)}{r_m^4} \sigma_{bm} \right]^{1/2} V_0 \exp(i\phi_m). \quad (20)$$

282 The first factor in (20), namely $[.]^{1/2}$, is copied from the square root of the radar equation (e.g.,
 283 Doviak and Zrnić 1984, p. 34) for power, where λ is the wavelength, and σ_{bm} is the back-scattering
 284 cross-section of each droplet. The function $G(\theta_m)$ is the gain function of the antenna at the droplet,
 285 which we have assumed to depend on its angle θ_m from the beam centerline. Two loss factors
 286 (< 1) have been included in (20): ℓ_w is the two-way waveguide loss and ℓ_B is the loss due to finite

bandwidth of the receiver; values assumed for the present study are given in Table 4. The last factor in (20), $\exp(i\phi_m)$, accounts for the phase shift induced by back-scattering at the m th droplet. The back-scattering cross-section and phase-shift (σ_{bm} and ϕ_m , respectively) will be discussed further in §2k.

Radar receivers have electronics that can obtain the real and imaginary parts (denoted I and Q) of $V(t)$ and compute the instantaneous received power

$$P_r(t) = I(t)^2 + Q(t)^2 = V(t)V^*(t). \quad (21)$$

We note in passing that $I(t)$ and $Q(t)$ are the components of the real part of $V(t)$ that are in-phase and 90° out-of-phase with the transmitted carrier, respectively. Substituting (18) into (21) and splitting the sum into two parts, following Doviak and Zrnić (1984, §4,1), gives

$$P_r(t) = \sum_{m,n} A_m A_n^* \exp[i(\omega_m - \omega_n)t] \exp[-2i(k_m r_m - k_n r_n)], \quad (22)$$

$$= \sum_m A_m A_m^* + \sum_{m,n,m \neq n} A_m A_n \exp[i(\omega_m - \omega_n)t] \exp[-2i(k_m r_m - k_n r_n)], \quad (23)$$

where $k_m \equiv \omega_m/c$. Arguments for using only the *first term* in (23) in order to evaluate reflectivity, i.e., for summing the powers received from each droplet, are given by Rayleigh (1945, p. 37), Beckmann (1962), and Doviak and Zrnić (1984, §4,1). The important point, which was phrased eloquently by Rayleigh, is that it is not correct to say that the power in a single return from a random distribution of droplets is the sum of the powers scattered by each. Rather, the result is true only when a *large ensemble of returns* from a statistically stationary target are averaged. This is most easily seen when we consider the case when all the A_m are equal (to unity, say). Then, the first term T_1 in (23) is $T_1 = N_d$. If droplet distances are randomly distributed in the resolution shell (assumed to be several wavelengths wide), then the magnitude of the second term will be the average of the summands times the number of terms, i.e., $T_2 \approx N_t^{-1/2} \times N_t = N_t^{1/2} \approx N_d$, where $N_t = N_d(N_d - 1)$ is the number of terms in the double sum. Hence both terms in (23) are of *similar*

307 *magnitude*. To make the second term smaller than the first, an ensemble average must be taken
 308 over many pulses. If the ensemble has N_s phase-uncorrelated samples, then the second term will
 309 be $N_s^{1/2}$ smaller than the first.

310 In the present application, the wake descends through the beam and so the target is not stationary,
 311 strictly speaking. In §3c we will explicitly verify that, for our case, an average of over a certain
 312 number of pulses does indeed yield the first term in (23). Note that a radar set does not have direct
 313 access to the first term in (23); only we as simulators do.

314 To provide a measure of detectability, we will present the signal-to-noise ratio

$$\text{SNR1} \equiv P_{r1}/P_{\text{noise}}, \quad (24)$$

315 where P_{r1} is the first term in (23) and the average noise power is

$$P_{\text{noise}} = k_B T_0 F_N / \tau, \quad (25)$$

316 where $k_B = 1.381 \times 10^{-23} \text{ J K}^{-1}$ is Boltzmann's constant, $T_0 = 290 \text{ K}$ is a reference temperature
 317 set by convention, and F_N is the overall noise figure of the chain of components in the receiving
 318 cascade. Values for F_N and τ are listed in Table 4 for each radar set.

319 Finally, since each computational droplet represents a multiplicity M_{actual} of actual droplets, we
 320 have

$$\sum_{m=1}^{N_d} \rightarrow M_{\text{actual}} \sum_{m=1}^{N_{\text{comp}}}, \quad (26)$$

321 where N_{comp} is the number of computational droplets in the resolution volume. Note that all M_{actual}
 322 copies of each computational droplet are assumed to be at the same location and therefore their
 323 scattered voltages at the receiver add constructively. This assumption does not bias SNR1 since
 324 its calculation involves summing individual scattered powers anyway. We claim that the statistics
 325 of individual pulse returns are also not affected by this assumption; this will be verified (§3d) in a
 326 computational test where the number of computational droplets is increased.

327 *h. Calculation of the doppler spectrum*

328 Radars calculate a doppler spectrum for a given spatial observation location by performing a Fast
 329 Fourier Transform (FFT) of complex voltage returns (at the same range gate) from a sequence of
 330 pulses separated by $\Delta t_{\text{pulses}} = 1/\text{PRF}$, where PRF is the pulse repetition frequency. We shall do the
 331 same for the simulations. From a series of pulse returns, V_n , $n = 0, 1, \dots, N_{\text{FFT}} - 1$, the normalized
 332 transform

$$\hat{V}(k) \equiv \frac{1}{N_{\text{FFT}}} \sum_{n=0}^{N_{\text{FFT}}-1} V_n e^{-i2\pi kn/N_{\text{FFT}}}, \quad k = 0, \dots, N_{\text{FFT}} - 1, \quad (27)$$

333 and then the power spectrum $S(k) \equiv \hat{V}(k)\hat{V}^*(k)$ is computed. Note that the frequency index k
 334 corresponds to an actual frequency

$$k_{\text{actual}} = \begin{cases} k, & k \leq N_{\text{FFT}}/2; \\ k - N_{\text{FFT}}, & N_{\text{FFT}}/2 < k \leq N_{\text{FFT}} - 1. \end{cases} \quad (28)$$

335 The frequency k_{actual} is in units of (the period of the sequence) $^{-1} = (N_{\text{FFT}}\Delta t_{\text{pulses}})^{-1}$, so in units of
 336 s^{-1}

$$f(k_{\text{actual}}) = \text{PRF } k_{\text{actual}}/N_{\text{FFT}}. \quad (29)$$

337 Equating this to $-2(u_{\text{doppler}}/c)f$ gives the doppler velocity associated with each k_{actual} . Finally,
 338 we state that we use the Hamming window (e.g., Harris 1978).

339 *i. Antenna gain function*

340 We assume a Gaussian beam with transmitted power flux (power per unit area) vector

$$\mathbf{S}_t = A \exp(-\theta^2/\theta_0^2) \hat{\mathbf{r}}, \quad (30)$$

341 where A is a coefficient, θ is the angle from the beam centerline, and

$$\theta_0 = \left(2\sqrt{\ln 2}\right)^{-1} \theta_b \quad (31)$$

342 in terms of the half-power full-width, θ_b . The total power crossing a sphere of radius r is

$$P_t = 4\pi r^2 \int_0^\pi \mathbf{S}_t \cdot \hat{\mathbf{r}} \sin \theta, d\theta = 2\pi r^2 \theta_0^2 A, \quad (32)$$

343 for a narrow beam. Using the definition of the gain function, $G(\theta)$, we obtain

$$G(\theta) \equiv \frac{4\pi r^2 S_t}{P_t} = \frac{2}{\theta_0^2} \exp(-\theta^2/\theta_0^2) \quad (33)$$

344 *j. Radars included in the study*

345 Table 4 lists parameters of currently operational doppler weather/cloud radars considered in the
 346 present study. The S, C, and X-band radars chosen are the DWSR series manufactured by EEC
 347 (Enterprise Electronics Corporation, Enterprise, Alabama). ARC (Advanced Radar Corporation,
 348 Boulder, Co.) makes quite similar C and X-band radars, while Baron Services (Huntsville, Al.)
 349 makes similar S, C, and X-band radars. The power and beamwidth values of the C-Band TDWR
 350 (Terminal Doppler Weather Radar) deployed at many US airports is subsumed by the range of
 351 values provided by the EEC C-band radar, and is therefore not included here.

352 A number of descriptions of Ka-band (35 GHz) cloud radars have appeared in the literature
 353 (Hamazu et al. 2003; G6rsdorf et al. 2015). In the present work, we use parameters of the MIRA-35
 354 radar manufactured by Metek (Elmshorn, Germany) which is described in G6rsdorf et al. (2015).
 355 This choice was motivated by its relatively high power (30 kW). Other Ka-band weather radars,
 356 operational at the time of writing are: (i) Scanning 2 kW radars operated by U.S. Department of
 357 Energy’s Atmospheric Radiation Measurement (ARM) Climate Research Facility (Widener et al.
 358 2012). (ii) The Copernicus 1 kW radar at Chilbolton Observatory (UK). (iii) An airborne 25
 359 kW multi-frequency (X, Ka, and W-band) radar developed by Prosensing that is being used by
 360 NASA’s Langley Research Center for research into the detection and avoidance of super-cooled
 361 water droplets.

362 The science and technology of W-band (94 GHz) radars for cloud and precipitation research is
 363 reviewed in Kollias et al. (2007). For the present work we chose the W-SACR radar, which has
 364 been developed by the U.S. Department of Energy’s Atmospheric Radiation Measurement (ARM)
 365 program (Widener et al. 2012; Kollias et al. 2014).

366 With increasing frequency, f , reflectivity increases as f^4 in Rayleigh’s formula (ignoring
 367 Mie-scattering corrections). Furthermore, the size of the antenna required to obtain the same
 368 beamwidth is reduced. The main drawback of high frequency is increased attenuation due to pre-
 369 cipitation between the radar and target. For example, the last entry in Table 4 gives the attenuation
 370 rate in medium rain at W-band as 7 dB/km. A compensating factor is that when there is precipi-
 371 tation, the ambient humidity is also very high and so there is minimal evaporation, and, if natural
 372 precipitation is present in the wake, it will also contribute to reflectivity.

373 *k. Mie cross-section and phase-shift*

374 Since we have can rather large droplets in the present application and frequencies up to 94
 375 GHz, the back-scattering cross-section and phase-shift are obtained using Mie’s formula instead
 376 of Rayleigh’s approximation. We used subroutine BHMIE, available from Prof. B.T. Draine’s
 377 website at Princeton University, and checked the results using subroutine MIEV0 developed by
 378 Dr. W.J. Wiscombe (NASA Goddard).

379 Some understanding of notation is required to properly use these routines. Let the incident field
 380 be of unit magnitude and polarized in the 2-direction (defined to be perpendicular to the plane
 381 containing the incident and observer directions). For a spherical target, the scattered field in the
 382 far-field is also polarized in the 2-direction and is given by

$$E_{s2}(r, \theta) = \frac{e^{ikr}}{kr} f_{22}(\vartheta), \quad (34)$$

where f_{22} is complex, $k = 2\pi/\lambda$, ϑ is the angle of the observer relative to the direction of propagation of the incident wave, and r is distance from the center of the sphere. The backscattering cross-section and phase shift are obtained as

$$\sigma_b \equiv 4\pi r^2 \frac{|\mathbf{E}_s(\pi)|^2}{|\mathbf{E}_i|^2} = \frac{4\pi}{k^2} |f_{22}(\pi)|^2, \quad (35)$$

$$\phi = \arg(f_{22}(\pi)). \quad (36)$$

At the start of the reflectivity calculation at a given frequency, we tabulate the ratio $\sigma_b/\sigma_{b,\text{Rayleigh}}$ and the difference $\phi - \phi_{\text{Rayleigh}}$ as a function of droplet radius a . Rayleigh's formulas are (Ishimaru 1978, p. 19)

$$\sigma_{b,\text{Rayleigh}} = 4|K_\varepsilon|^2 (ka)^4 (\pi a^2), \quad (37)$$

$$\phi_{\text{Rayleigh}} = \arg(K_\varepsilon), \quad (38)$$

where K_ε (a complex number) is given by

$$K_\varepsilon = \frac{\varepsilon - 1}{\varepsilon + 2}. \quad (39)$$

The quantity $\varepsilon(f, T)$ is the complex dielectric constant of water; our convention of $e^{+i\omega t}$ for the time dependence requires the imaginary part of ε be positive for an absorbing material. It is a function of frequency and temperature and was evaluated using the single Debye model of Liebe et al. (1991) as implemented in subroutines available from Prof. Chris O'Dell's website at Colorado State University. Since the droplet temperature is almost the same for all drops (the spread was 4 C at most), the dielectric constant ε is evaluated at the average temperature of all the drops in the trail.

Figure 2 displays the Mie back-scattering cross-section σ_b (normalized by the Rayleigh value) and phase-shift ϕ as a function of droplet radius at the five frequencies considered in this work.

399 At the largest radii in this work, $a \approx 600 \mu\text{m}$, the error in using Rayleigh's cross-section is about
400 20% at 35.1 GHz.

401 *l. Choice of ambient temperature and humidity*

402 Droplet evaporation calculations require specification of the ambient temperature and humidity.
403 For guidance on appropriate choices, METARs (Meteorological Aerodrome Reports) during 2000-
404 2014 were downloaded from

405 <http://mesonet.agron.iastate.edu/request/download.phtml>

406 and processed for the five busiest airports in the U.S. Figures 3a and b show the monthly-averaged
407 temperature and relative humidity (RH), respectively, when IFR conditions prevailed. Figure 3c
408 shows the percentage of reports that fall into the IFR category. One sees that the average RH is
409 always above 90%. To further synthesize this data, yearly averages were taken (Table 5). Among
410 the five airports, LAX has the highest rate of evaporation in IFR conditions on average since it
411 is the warmest and driest on average. Our choice is the IFR average for LAX, namely, $T = 15.2$
412 C and $\text{RH} = 92.7\%$. Looking at the monthly data for the other four airports, this appears to be a
413 reasonable choice for them also: it is an approximate lower bound for their monthly RH and their
414 temperature is higher only during the summer months when IFR reports are low.

415 Since it is expensive for flight tests to wait for IFR conditions to occur, and it is desirable to have
416 a wake sensor that can work in a wider variety of atmosphere conditions, we will also consider a
417 case of lower humidity and higher temperature, namely, $\text{RH} = 60\%$ and $T = 20 \text{ C}$.

418 *m. Radar placement with respect to the wake*

419 Here, we choose the radar location $(x_{\text{rad}}, y_{\text{rad}}, z_{\text{rad}})$ in aircraft-centered coordinates. Based on
420 current wake separations (Table 1), it should not be necessary to examine a wake more than 6 nm

421 behind the aircraft. We therefore chose to present results for the reflectivity at $x = 6$ nm, the worst
 422 case for droplet loss by evaporation and sedimentation. The radar is also placed at $x_{\text{rad}} = 6$ nm so
 423 it can view the $x = 6$ nm wake cross-section at normal incidence. Next, we assume that the aircraft
 424 is at the touchdown point. At 6 nm from the touchdown point, the altitude of an aircraft flying a
 425 3° glide slope is $H = 582$ m. Therefore, the vertical coordinate of the radar is $z_{\text{rad}} = -582$ m. For
 426 purposes of this study, we assume an aircraft flying straight and level at this altitude. Initial flight
 427 tests would also presumably have the aircraft fly straight and level. In this case, since the vortex
 428 pair descends at a speed of $W_{\text{desc}} = 1.75 \text{ m s}^{-1}$, its axis makes a downward angle of 1.7° relative to
 429 the horizontal. For an aircraft on a 3° glideslope, the vortex axis would therefore be 1.3° upward
 430 from the wing. This difference in the angle of the wake axis is expected to have a very small effect
 431 on reflectivity.

432 To place the radar laterally with respect to the wake, we imagine several parallel approaches that
 433 are monitored by the same radar. The largest separation between parallel runways is about 5000
 434 ft (Doyle and McGee 1998). At 6 nm from touchdown, the lateral width of the ILS (Instrument
 435 Landing System) approach is 3182 ft for a standard 5° splay, and we imagine an aircraft that has
 436 strayed to the outer edge of this zone. If the radar is placed in the middle of the two furthest
 437 runways we obtain a lateral distance of 0.67 nm. In the presence of a crosswind, we imagine that
 438 the wake would be monitored for as long as it remained between the outer edges of the left and
 439 right ILS zones. In conclusion, we select $(x_{\text{rad}}, y_{\text{rad}}, z_{\text{rad}}) = (6 \text{ nm}, -0.67 \text{ nm}, -582 \text{ m})$ relative to
 440 the aircraft.

441 The elevation angle of the radar beam from this location varies between 10.6° and 17.1° as the
 442 scanned range of z on the wake center plane varies between $z = -350$ and -200 m (see Figure 4).
 443 Since the beamwidth of the radar likely to be used is $\leq 1^\circ$, ground reflection will be small. To
 444 significantly reduce ground and structure clutter, the radar can be placed directly under the flight

445 path. This would require a separate radar for each parallel runway. Another issue is loss of radar
 446 sensitivity at smaller ranges; for MIRA-35 this happens for $r < 360$ m (Matthias Bauer-Pfundstein,
 447 private communication). However, this loss is probably offset by the increase in power from the
 448 r^4 factor in Equation (20).

449 3. Results

450 a. Signal-to-noise ratio for the IFR case

451 We begin by considering IFR ambient conditions ($RH = 92.7\%$, $T = 15.2$ C) chosen as described
 452 in §2l. Nozzle 1 from Table 2 is used and parameters for the injected square of droplets, described
 453 in §2e, are $n_{\text{square}} = 15$, $n_x = 120$, and $w_{\text{square}} = 1$ m. Figure 4 shows simulated values of SNR1,
 454 calculated using (24), for the five radars listed in Table 4. Each SNR1 plot is an instantaneous
 455 range-elevation scan of the $x = 6$ nm cross-section of the wake and each location on the plot corre-
 456 sponds to the mid-radius of a resolution shell along the beam centerline. The pulse width is chosen
 457 to be $\tau = 0.2 \mu\text{s}$ for all the radars except for DWSR-8501S, in which case the lowest available τ of
 458 $0.4 \mu\text{s}$ is used. Droplets in a 30 m thick axial slab centered at $x = 6$ nm are shown in panel (a). Due
 459 to centrifugation, larger droplets lie at greater distances from the vortex center, which is devoid of
 460 droplets. The very large particles sediment due to gravity after being centrifuged. Except for the
 461 S-band radar, all radars give $\text{SNR1} > 10$ dB at most points surrounding the vortices; the reflectivity
 462 is higher for the higher frequency radars. The W-SACR radar gives the highest reflectivity despite
 463 having the smallest pulse power.

464 For all radars, there is a drop in reflectivity near the 2 o'clock and 4 o'clock positions for the
 465 left vortex (8 and 10 o'clock positions for the right vortex). This manifests as a crescent-wrench
 466 shaped reflectivity pattern that is most prominent for the DWSR 2001X radar. How this feature is

467 related to the droplet configuration, which in turn is related to the vortex flowfield, remains to be
468 elucidated.

469 Figure 5 shows that with its lowest available pulse width of $0.05 \mu\text{s}$, the W-SACR radar is able
470 to resolve some of the spiral structure of the droplet pattern at the expense of some loss in SNR1.

471 *b. Insensitivity to initial condition*

472 To test sensitivity to initial conditions, instead of injecting droplets in a regular grid pattern
473 on each square, droplets were randomly placed in the squares. Figures 6a and b show that both
474 the droplet configuration at $x = 6 \text{ nm}$ as well SNR1 for DWSR-2001X are changed very little;
475 compare with Figures 4a and d. We expect this to be true for all the radars as well. In another test
476 (Figure 6c and d), the width of the square, w_{square} , was reduced from 1 m to 50 cm, keeping the
477 number of droplets fixed. This increases the initial number density in the cross-plane (yz) and, to
478 keep the spacing the same in the streamwise (x) direction, the injection interval Δt_{inject} was also
479 halved. One might think that this would increase the number density downstream. However, the
480 flow tends to both reduce number density (where there is rotation) and increase it (where there
481 is strain), and eventually, the number density tends to a distribution that is mostly independent of
482 initial condition.

483 *c. Pulse to pulse fluctuation and averaging*

484 The SNR1 results in §3a were based on using the first term in Equation (23), which sums the
485 powers reflected by individual droplets. It was argued that for a statistically stationary target, this
486 should equal the average power from many pulses. In the present case, the droplet configuration
487 is not spatially homogeneous and is descending through a fixed beam. Hence, the question arises
488 whether the powers returned from a sequence of pulses can be considered to be statistically sta-

tionary in a certain interval, and if so, how many pulses is sufficient to recover the SNR1 values presented.

To obtain complex voltage returns from a sequence of pulses one needs to evolve the wake in time, however, the method that was described in §2 gives a trail of droplets at a single instant of time, t . To evolve this configuration to time $t + \Delta t$, the configuration at t is translated horizontally by $\Delta x = -U_{\text{app}}\Delta t$, i.e., the droplet trail is assumed to be invariant in a reference frame moving to the left with the airplane. This procedure does not correspond exactly to reality, but captures both the rotation of droplets around the vortices, and their vertical descent with time at a fixed location. The received complex voltage is evaluated using (18) at a sequence of times separated by the pulse repetition period, keeping the resolution volume centered at $(x, y, z) = (6 \text{ nm}, -50 \text{ m}, -230 \text{ m})$. This location corresponds to the upper SNR1 peak of the crescent wrench in Figure 4. The value of the pulse repetition frequency (PRF) was chosen to be at or close to the highest value available for each radar.

Figure 7 shows the result for a time period during which a cluster of droplets enters and leaves the beam. The power in individual pulse returns is shown in gray. The total number of active pulses changes from radar to radar because their beam widths and PRFs are different. In particular, the period of activity was found to equal the time it would take the vortex pair to descend through roughly one-third of the vertical projection of the half-power beam width. The average of pulse powers is shown in green over an averaging segment whose length is 512 pulses. The red curve shows the value of SNR1. Our assumption was that SNR1 should equal the green level. This is seen to be true to a good degree. The fluctuations are due to statistical error and were found to decrease with increasing the averaging interval. It is worth remembering here that the radar has access to only the individual pulse returns and their average (for example the green values); only the simulation has access to the red curve (SNR1).

513 *d. Convergence of pulse statistics*

514 Recall that each computational droplet at a single location represents M_{true} actual droplets lo-
 515 cated at different positions; in fact $M_{\text{true}} \approx 100$ in the calculations presented. It was claimed (§2g)
 516 that this should not affect pulse statistics, provided the number of computational droplets is suffi-
 517 ciently large. To verify this, the number of computational droplets was increased by four. Random
 518 placement of droplets was employed in the injected squares. Four realizations of the droplet trail
 519 were generated using different random number seeds for the initial size distribution and droplet
 520 placement. The four realizations were then merged into one trail for the radar reflectivity calcula-
 521 tion. Figure 8 shows that the probability density $p(|V|)$ of the modulus $|V|$ of complex voltage is
 522 unchanged by the resolution refinement. The probability densities are very well fit by the Rayleigh
 523 distribution (Beckmann 1962)

$$p(|V|) = \frac{|V|}{\sigma_R^2} \exp(-|V|^2/2\sigma_R^2), \quad (40)$$

524 having the same mean as the data. The Rayleigh distribution results when the scattering amplitude
 525 is the same for all droplets and the phases uniformly distributed. The case selected is the same
 526 as that shown in Figure 7d (apart from the random placement of droplets in the injected squares).
 527 Pulses in the interval of stationarity were chosen, namely pulse number $\in [-8000, 8000]$.

528 *e. A non-IFR condition*

529 It would be valuable to have the capability to detect wakes in non-IFR conditions. Furthermore,
 530 in a flight test study of the feasibility of the present proposal, it would be too costly to wait until
 531 IFR conditions occur before a test can be conducted. For this reason it is of interest to know what
 532 reflectivity is obtained at less humid and less cold conditions. We chose $\text{RH} = 60\%$ and $T = 20^\circ\text{C}$.

533 With the previous choice of $n_{\text{square}} = 15$ and $n_x = 120$ as injection parameters, it was found that
 534 a high rate of evaporation resulted in a small number of computational droplets remaining near
 535 $x = 6$ nm. This increased statistical error. To reduce sampling error, an ensemble of ten trails
 536 were computed with different random number seeds for the droplet size sample. The ensemble
 537 was then combined into a single trail for the reflectivity analysis. As a result, the total number of
 538 computational droplets is so large that each one presents only 9.8 true droplets in the reflectivity
 539 analysis.

540 Figure 9 shows that only the high-frequency radars, MIRA-35 and W-SACR, give positive values
 541 of SNR1 (dB) in the vicinity of the vortices, and even these values are marginal. To increase SNR1,
 542 the number of nozzles could be increased; for instance four nozzles on each side of the aircraft
 543 would increase SNR1 by 6 dB.

544 There is a powerful method that enables detection even when $\text{SNR1 (dB)} < 0$. It comes at the
 545 cost of increased dwell and processing time. We learnt about the method from notes on the sen-
 546 sitivity of the MIRA-35 radar given to us by Matthias Bauer-Pfundstein (Metek). It is also briefly
 547 described in Görsdorf et al. (2015, p 680). The idea is that in a discrete Fourier transform, the
 548 noise is spread equally to all the frequency bins, whereas the spectrum of the signal is confined to
 549 only a few of the bins. (The latter is true provided the probability distribution of droplet velocities
 550 in the resolution cell is narrow compared to $2U_{\text{max}}$ for the radar. For MIRA- 35, for example, at
 551 $\text{PRF} = 10$ kHz we have $2U_{\text{max}} = 42 \text{ m s}^{-1}$ and so this is unlikely to be an issue.) Hence, an FFT
 552 effectively reduces the noise by a factor of N_{FFT} .

553 To investigate this technique, complex white noise with a mean power equal to P_{noise} for the radar
 554 was added to complex voltages of pulse returns. Illustrative results are shown in Figure 10. Panels
 555 (a) and (b) are for a range cell centered at the left white dot in Figure 9e where $\text{SNR1} = -2.7$
 556 dB. Panels (c) and (d) are for the right white dot where SNR1 is even lower, namely, -7.2 dB.

557 Consider panels (a) and (b). An averaging of pulse power returns by the radar would give values
558 (the green line) only slightly above the noise, not enough for a positive detection. Averaging the
559 doppler spectra from 10 segments gives panel (b) with a peak 40 dB above the noise. In the present
560 example, this would require a dwell time of 0.5 s for each elevation angle. For the second location
561 where SNR1 is weaker, the doppler spectrum has a peak that is about 25 dB above the noise (using
562 the same dwell time).

563 *f. Power-weighted average radial velocity*

564 It has been stated (Doviak and Zrnić 1984, §5.2) that the first moment of the doppler spectrum is
565 the radial velocity of droplets in the resolution volume, weighted by their individual scattered pow-
566 ers. This is reasonable although we have neither encountered nor attempted a proof of it starting
567 from Equation (2). Figure 11 displays the power-weighted average radial velocity corresponding
568 to the cases previously shown in Figure 4. Only points where SNR (dB) > 0 are shown. The
569 actual radial velocity (with respect to the radar) of the gas is shown in panel (f). The radar data
570 appears as a filtered version of the actual velocity and, due to particle centrifugation, is unable to
571 detect the maximum value of 19.8 m s^{-1} in the vortex core. Nevertheless, the radars give a good
572 representation of the gas velocity where particles are present. To estimate vortex circulation, the
573 observed velocity is multiplied by $2\pi r$ where r is the distance from the vortex center and can be
574 determined from the location of zero radial velocity.

575 *g. Effect of vortex core growth*

576 The vortex model presented in §2f assumed that the vortex core radius does not grow with down-
577 stream distance. In reality, the core radius grows and the peak velocity diminishes. Experiments
578 on aircraft wakes (see Govindaraju and Saffman 1971) have shown that the core radius, r_1 , defined

579 to be the radius where the tangential velocity peaks, diffuses as follows with distance x behind the
 580 plane:

$$r_1 = b_1 \left[\frac{(x - x_0)\Gamma}{U_{\text{app}}} \right]^{1/2}, \quad (41)$$

581 where b_1 is a constant that depends on the vortex Reynolds number, Γ/ν . In the present case
 582 $\Gamma/\nu = 3.5 \times 10^7$, or which Table I in Govindaraju and Saffman (1971) gives $b_1 = 1.3 \times 10^{-2}$
 583 (using the corrected value listed in their table). The value of the parameter x_0 (called the virtual
 584 origin) can be obtained from the core radius at $x = 0$. Plotting the profile we find that $r_1 = 0.8$ m
 585 for the present case which gives $x_0 = -558.8$ m.

586 To include core growth in the vortex model of §2f, the variable η is redefined as

$$\eta \equiv \frac{r}{g(x)b_0}, \quad (42)$$

587 where g is the growth function

$$g(x) = \frac{r_1(x)}{r_1(0)} = \left(\frac{x - x_0}{-x_0} \right)^{1/2}. \quad (43)$$

588 Figure 12 displays the decay of peak tangential velocity from $x = 0$ to $x = 6$ nm.

589 Figures 13a and b show the droplet configuration and SNR1, respectively, for the MIRA-35 radar
 590 when core growth is included; they should be compared with Figures 4a and e. This comparison
 591 shows that slightly less centrifugation takes places with core diffusion which makes the region of
 592 reflectivity slightly smaller.

593 *h. Comparison of four nozzles*

594 Finally, Table 6 compares SNR1 reflectivity for the four nozzles listed in Table 2. The range
 595 cell for all cases is centered at $(x, y, z) = (6\text{nm}, -50\text{m}, -230\text{m})$, which corresponds to the top of
 596 the crescent wrench in Figure 4. IFR ambient conditions have been assumed. It is observed that
 597 the quantity $\zeta_{\text{nozzle}}^<$ (defined in Equation 9), which depends only on the droplet size distribution

598 produced by a nozzle, provides an excellent indicator of the relative performance of different
599 nozzles.

600 To provide further insight we compute the quantity ζ_x which is defined to be ζ (see Equation
601 8) per unit axial length of the wake. It is calculated as a diagnostic of the droplet trajectory and
602 size evolution and is shown in Figure 14. The solid lines give the total value (over an entire cross-
603 section) and diagnose total evaporative loss. The dashed lines give the contribution from droplets
604 in a neighborhood (defined in the caption) of the vortex: these curves diagnose both evaporative
605 loss and loss by sedimentation. The ordering of ζ_x values (pertaining to the neighborhood of the
606 vortex) at $x = 6$ nm, which are also listed in the last column of Table 6, matches the ordering of
607 SNR1 for the different nozzles.

608 All statements of comparison in the following are relative to nozzle 1 and make reference to
609 Figure 14a. If the increased SNR1 reflectivity of nozzle 2 were due to increased volume alone, we
610 would get a 2.4 dB increase in reflectivity. The actual increase is 1.03 dB. To understand this, we
611 first observe that nozzle 2 (solid red line) initially has a 0.7 dB higher value of ζ_x , less than the 2.4
612 dB increase in its volume flow-rate. This is because nozzle 2 produces more small droplets. By
613 $x = 6$ nm the 0.7 dB increase has been reduced to 0.55 dB because the smaller droplets of nozzle
614 2 evaporate faster. The fact that ζ_x in the vicinity of the vortex is 0.6 dB higher must arise from
615 the fact that the smaller droplets of nozzle 2 have sedimented less.

616 Consider nozzle 3 (green curves). If its smaller reflectivity (relative to nozzle 1) were due
617 to decrease in volume, then we would expect a -0.91 drop in SNR1 which is close to what is
618 obtained. This is understandable given that its initial ζ_x is very nearly the same as for nozzle 1.
619 This is surprising given that nozzle 3 has many more smaller droplets. However, close inspection
620 of its size distribution (green line in Figure 14b) shows that it also has more droplets that are very
621 large (specifically $a > 370$ μm). This fact also explains the more rapid loss of ζ_x by sedimentation

622 (dashed green curve in Figure 14a) and less rapid loss by evaporation (solid green curve). Overall,
623 these two effects balance and the final effect that remains is that due to volume decrease.

624 Despite its smaller flow-rate, nozzle 4 has a higher initial value of ζ_x ; see the solid blue curve.
625 This is because it produces more large droplets. Unfortunately, they rapidly fall out of the wake
626 (dashed blue curve).

627 **4. Concluding Remarks**

628 It was proposed that spraying a small amount of water into the vortex wake of a heavy aircraft
629 during landing can make the wake visible to existing weather/cloud radars and thereby aid air
630 traffic controllers in selecting appropriate aircraft separations. This approach could also be used
631 for wake vortex studies of aircraft.

632 Simulations of the radar reflectivity of the spray trail were performed for existing weather/cloud
633 radars. For ambient humidity at the lower end of values typical for IFR conditions, the results
634 showed that that good signal-to-noise (SNR) ratios (averaged over many pulses) are obtained at
635 distances behind the aircraft of up to 6 nm, the largest that would be contemplated given existing
636 wake separations used in air traffic control. For the case most studied here, the amount of water
637 spray was 3 gallons per nautical mile of wake that needs to be detected. A currently available
638 nozzle used for agricultural spraying can be used. A doubling of volume by doubling the number
639 of nozzles gives a proportional increase in SNR. For a case of average humidity, evaporation for
640 severe and pulse-averaged, SNR values dropped below unity. However, since the pulse returns of
641 the wake remained statistically stationary for 1 to 6 secs (depending on the radar), it was shown that
642 the signal-to-noise ratio can be increased to detectable levels by spectral (doppler) processing and
643 averaging doppler spectra for consecutive time segments. This would require greater dwell time

644 for each direction the radar is pointed at. Ultimately, selecting the dwell time for a given situation
645 will be a trade-off between quickly completing a scan of a wake cross-section and increasing SNR.

646 1. Suggested future work

647 (a) As an airplane nears the touch-down point, flaps are deflected at increasing angles. The
648 presence of flap vortices should be included in future analysis.

649 (b) The present work has ignored space-time fluctuations of the air velocity field. They will
650 arise from the direct effect of atmospheric turbulence and from vortex core waviness
651 induced by atmospheric turbulence, and further amplified by vortex core instabilities.
652 Velocity fluctuations will disperse the spray trail and if this happens on the scale of
653 the pulse width or beam width, then reflectivity will be reduced. This effect should be
654 studied in future work.

655 2. Application notes

656 (a) For the purposes of simulation we generated a spray trail that was 7 nm long. In practice,
657 to reduce the volume of water, spray would be released only at axial locations where a
658 detection would be performed. For each detection location, the length of the trail would
659 need to be a few beam widths long and the release location would have to account for any
660 head/tail wind. A trail that is three beam widths long would require only 0.084 gallons.
661 This value assumes that $\theta_b = 1^\circ$, range = 1 km, and a flow-rate of 3 gallons nm^{-1}
662 (counting both sides of the airplane). Hence, there is considerable room for increasing
663 water volume, and therefore signal-to-noise ratio. The main difficulty is that for the
664 nozzles presently considered, more than one would be required. A better solution might
665 be to design a spray head containing several nozzles.

- (b) Given that spectral processing is required for detection in conditions of average humidity, it is likely that processing decisions will have to be based on humidity or on the quality of incoming returns. If the humidity is high and the quality of returns high, then the mean velocity can be obtained from a pulse-pair estimate. If the humidity is low, then spectral processing can be turned on.
- (c) Some of the requirements of the present application are similar to those for radar imaging of tornados (French et al. 2014). This includes a smaller detection volume and the need to complete a scan faster than the vortex evolution time. Therefore the technology developed for that application could be useful here.
- (d) In IFR conditions, natural precipitation (fog, mist, drizzle, or heavy rain) will be present between the radar and the wake and lead to absorption. However, at ranges of ≈ 1 nm envisioned for the present application, this is small.
- (e) If spraying is to be employed in very cold conditions (Denver, Colorado comes to mind), freezing of water must obviously be prevented in the water storage and delivery system.
- (f) *Dual polarization.* Droplets moving relative to the air become oblate due to a higher air pressure at the front stagnation point and low pressure at 90° from the front stagnation point. For falling rain droplets, this results in greater reflected power from incident waves that are horizontally versus vertically polarized (Doviak and Zrnić 1984, §8.5.3). Most weather radars employ dual polarization to obtain more information about rainfall rate. Since, in the present case, droplets revolving around the vortices are small and their velocity relative to the air is also small, we expect that droplets will remain very nearly spherical. Therefore, it is not expected that dual polarization would provide additional information about the flow. However Keränen and Chandrasekhar (2014)

have suggested that dual polarization could be used for enhancing SNR. This works by exploiting coherence between signals in the horizontal and vertical channels.

(g) Since the maximum range pertinent to the present application is much lower than for cloud and precipitation detection, the pulse repetition frequency could be increased (the maximum duty cycle of the klystron or magnetron permitting) in order to reduce the dwell time for spectral averaging.

(h) One obvious modification of existing cloud/precipitation radar software for the present application would be a reduction in the spacing of range gates from their current values, for example 25 m which is employed in Ka-SACR and W-SACR (Kollias et al. 2014).

Acknowledgments. I am grateful to several individuals for sending me information when requested and sometimes more information than requested. Matthias Bauer-Pfundstein (Metek) sent me information on the MIRA-35 radar including a detailed dBZ sensitivity calculation, information on signal processing, and detailed information on loss determination. It was from his dBZ sensitivity document that I learnt that a discrete Fourier transform enhances signal-to-noise ratio in the spectral bin of interest. John Cho (MIT Lincoln Laboratories) sent me information on the TDWR (Terminal Doppler Weather Radar). Brad Fritz (U.S. Dept. of Agriculture) sent me his Excel program giving parameters of the droplet size distribution produced by different aerial spray nozzles at different free-stream air speeds. He also experimentally measured for me the flowrate of the Davidon-Triset nozzle. Calvin Kroes (CP Products) sent me information on nozzle orifice areas, flow rates, and exit velocities for various CP nozzles. Keith Vickers (Enterprise Electronics Corporation) sent me basic information on the DWSR series of radars. I am grateful to Alan Wray (NASA Ames) for useful discussions. I am grateful to Jasim Ahmed and Alan Wray for performing the internal review.

APPENDIX

Both the sub-sections below use the abbreviation PK for the book by Pruppacher and Klett (1997). The subscripts ‘a’ and ‘w’ denote air and water, respectively.

A1. Drag coefficient

With the Reynolds number defined as $\text{Re} \equiv 2a|\mathbf{u}_{\text{rel}}|/\nu_a$ (where ν_a is the kinematic viscosity of air), the coefficient of drag, C_D , is obtained by numerically inverting the relation (PK, Equation 10-145):

$$Y = \sum_{m=0}^6 B_m X^m, \quad (\text{A1})$$

where $X = \ln(C_D \text{Re}^2)$ and $\text{Re} = \exp(Y)$. This formula is originally from Beard (1976) and is based on the drag coefficient of a solid sphere. The validity of this rests on two assumptions. The first is that the droplet does not distort significantly from being spherical. The equilibrium aspect ratio of a falling raindrop is given by PK (Equation 10-108):

$$\frac{b}{a} = \frac{1 - 0.11\text{We}}{1 + 0.11\text{We}}. \quad (\text{A2})$$

Here $\text{We} \equiv 2a\rho_a u_{\text{rel}}^2/\gamma_{w/a}$ is the Weber number, where $\gamma_{w/a}$ is the surface tension of water in air. For nozzle 1 and the IFR case, the smallest value of b/a was 0.9 which occurred at early times for a droplet which quickly fell below the vortex. We conclude that droplet deformation is negligible particularly for those droplets that remain with the vortex pair. The second assumption is that the ratio of dynamic viscosities, $\eta_a/\eta_w \approx 1.8 \times 10^{-2}$ is small. In the creeping flow limit, the Hadamard-Rybczynski formula (see Beard 1976) for the drag of a water sphere divided by the drag of a solid sphere is

$$\frac{F_D}{F_{Ds}} = 1 - \eta_a/3\eta_w = 0.995. \quad (\text{A3})$$

730 Numerical solutions (PK, p. 388) indicate that for $Re < 300$, the drag coefficient of a water sphere
731 differs by less than $\sim 1\%$ from that of a solid sphere.

732 Formula (A1) is valid for $Re < 500$. Only for nozzle 4 was this condition slightly exceeded for
733 a few droplets. For $Re \leq 1.5$, the explicit formula for solid spheres (White 1974, eq. 3-265) was
734 found to agree well with (A1) and was used instead. We have also implemented but not used the
735 Schiller and Naumann explicit drag formula for a solid sphere (e.g., Apte et al. 2003)

$$C_D = \frac{24}{Re} \left((1 + 0.15Re^{0.687}) \right) \quad (A4)$$

736 which is said to be accurate to within 5% for $Re < 800$. Figure 15 compares the three formulas
737 for C_D up to the maximum value of $Re = 800$ we allow in the code. It suggests that in the future
738 it would be as accurate to use the explicit Schiller and Naumann formula, which is cheaper to
739 compute.

740 **A2. Evaporation model**

741 The evaporation model uses appropriate formulas from PK. These formulas are collected here
742 to document the choices we have made and also because they are scattered throughout the book.
743 Gas kinetic effects and the Kelvin curvature effect are neglected since we remove droplets when
744 their radii fall below $20 \mu m$. Throughout, T_C denotes centigrade temperature:

$$T_C = T - 273.15. \quad (A5)$$

745 Note that there are 100 Pa in a mb. Subscripts ‘a’ and ‘w’ denote air and water, respectively.

746 *a. Properties of air, liquid water, and water vapor*

747 Given the universal gas constant, $\mathcal{R} = 8.3144 \text{ J K}^{-1} \text{ mol}^{-1}$, and the molar mass of dry air,
748 $M_a = 28.9644 \times 10^{-3} \text{ kg mol}^{-1}$, the gas constant for air is

$$R_a = \mathcal{R}/M_a. \quad (\text{A6})$$

749 The density of air is calculated from the ideal gas law:

$$\rho_a = p/R_a T. \quad (\text{A7})$$

750 The density of liquid water at $p = 1 \text{ atm}$ is given by (PK 3-13):

$$10^3 \rho_w = \frac{\sum_{m=0}^5 A_m T_C^m}{1 + BT} \text{ g cm}^{-3}, \quad 0 \leq T_C \leq 100, \quad (\text{A8})$$

751 with $A_0 = 999.8396, A_1 = 18.224944, A_2 = -7.922210 \times 10^{-3}, A_3 = -55.44846 \times 10^{-6}, A_4 =$
752 $149.7562 \times 10^{-9}, A_5 = -393.2952 \times 10^{-12}, B = 18.159725 \times 10^{-3}$. The thermal diffusivity of
753 air is

$$\kappa_a = k_a/\rho_a C_p, \quad (\text{A9})$$

754 where the conductivity is given by (PK 13-18a):

$$k_a = (5.69 + 0.017 T_C) \times 10^{-5} \text{ cal cm}^{-1} \text{ s}^{-1} \text{ K}^{-1}. \quad (\text{A10})$$

755 Note that there are 4.184 J per cal. The heat capacity of air is:

$$C_p = 1006.1 \text{ J kg}^{-1} \text{ K}^{-1}. \quad (\text{A11})$$

756 The diffusivity, D_v , of water vapor is calculated using Equation (PK 13-3):

$$D_v = 0.211 \left(\frac{T}{T_0} \right)^{1.94} \left(\frac{p_0}{p} \right) \text{ cm}^2 \text{ s}^{-1}, \quad (\text{A12})$$

757 with $T_0 = 273.15 \text{ K}$ and $p_0 = 1013.25 \text{ mb}$. The dynamic viscosity of air is (PK 10-141)

$$\eta_a = (1.718 + 0.0049 T_C) \times 10^{-4} \text{ poise}, \quad T_C \geq 0. \quad (\text{A13})$$

758 The Schmidt number of vapor is defined (PK , p. 538) as

$$Sc_v \equiv \nu_a / D_v, \quad (A14)$$

759 where $\nu_a = \eta_a / \rho_a$ is the kinematic viscosity. The Schmidt number for heat is

$$Sc_h \equiv \nu_a / \kappa_a. \quad (A15)$$

760 *b. Evolution of droplet radius*

761 The evolution of droplet radius $a(t)$ is given by:

$$a \frac{da}{dt} = \left(a \frac{da}{dt} \right)_0 f_v, \quad (A16)$$

762 where f_v , called the ventilation coefficient, represents the enhancement of evaporation rate due to
763 advection of air past the droplet, and $(\)_0$ represents a quantity in the absence of advection.

764 Let $Re = 2aU_{rel}/\nu_a$ denote the Reynolds number based on droplet diameter and drop speed U_{rel}
765 relative to the air. Defining $F \equiv Sc_v^{1/3} Re^{1/2}$, the ventilation coefficient is given by (PK 13-60) and
766 (PK 13-61):

$$f_v = \begin{cases} 1.00 + 0.108F^2, & F < 1.4; \\ 0.78 + 0.308F, & 1.4 \leq F < 51.4. \end{cases} \quad (A17)$$

767 The first factor on the RHS of (A16), which represents evaporation in the absence of advection, is
768 given by

$$\left(a \frac{da}{dt} \right)_0 = \frac{D_v M_w}{\mathcal{R} \rho_w} \left(\frac{e_\infty}{T_\infty} - \frac{e_{sat}(T_a)}{T_a} \right), \quad (A18)$$

769 where D_v is the vapor diffusivity (which we evaluated at ambient conditions using equation A12),
770 $M_w = 28.97 \text{ gm mol}^{-1}$ is the molecular mass of water, e_∞ is the vapor pressure in the ambient, T_∞
771 is the ambient temperature, and $e_{sat}(T_a)$ is the saturation vapor pressure evaluated at the surface

772 temperature T_a of the droplet. For $e_{\text{sat}}(T)$ we use the expression (Sonntag 1994, eq. 7)

$$e_{\text{sat}}(T) = 100 \exp \left(\sum_{m=1}^4 a_m T^{m-2} + a_5 \ln T \right) \text{ Pa}, \quad 173.15 \leq T \leq 373.15, \quad (\text{A19})$$

773 with $a_1 = -6.0969385 \times 10^3$, $a_2 = 1.6635794 \times 10^1$, $a_3 = -2.711193 \times 10^{-2}$, $a_4 = 1.673952 \times$
 774 10^{-5} , $a_5 = 2.433502$.

775 *c. Temperature at the droplet surface*

776 The internal energy of the water droplet is:

$$q = m C_w T_a, \quad (\text{A20})$$

777 where m is its mass, $C_w = 4.187 \times 10^3 \text{ J kg}^{-1} \text{ K}^{-1}$ is the heat capacity of water, and T_a is its
 778 temperature, which we have taken to be uniform and equal to the value at the surface. The internal
 779 energy of the drop increases due to diffusion of heat at its surface and release of latent heat (PK
 780 13-65):

$$\frac{dq}{dt} = 4\pi f_h a k_a (T_\infty - T_a) + L_e \frac{dm}{dt}, \quad (\text{A21})$$

781 where L_e is the latent enthalpy of evaporation of pure water evaluated at the surface temperature
 782 of the drop. The dependence of L_e on centigrade temperature T_C is:

$$L_e = (2500.8 - 2.36 T_C + 0.0016 T_C^2 - 0.00006 T_C^3) \times 10^3 \text{ J kg}^{-1}. \quad (\text{A22})$$

783 Substituting (A20) into (A21) gives

$$\frac{dT_a}{dt} = \frac{3 f_h k_{a\infty}}{C_w a^2 \rho_w} (T_\infty - T_a) + 3 (L_e / C_w - T_a) \frac{1}{a} \frac{da}{dt}. \quad (\text{A23})$$

784 Here f_h is the ventilation coefficient for heat: it is given by the same expression as (A17) except
 785 with $F = \text{Sc}_h^{1/3} \text{Re}^{1/2}$, where Sc_h is the Schmidt number for heat.

References

- Apte, S., M. Gorokhovski, and P. Moin, 2003: LES of atomizing spray with stochastic modeling of secondary breakup. *Intl. J. Multiphase Flow*, **29**, 1503–1522, doi:10.1016/S0301-9322(03)00111-3.
- Babaresco, F., 2012: Radar/lidar sensors for wind & wake-vortex monitoring on airport: First results of SESAR P12.2.2 XP0 trials campaign at Paris CDG airport. <http://www.wakenet.eu/index.php?id=185>, Presentation slides for 4th Major Workshop of WakeNet3-Europe.
- Babaresco, F., J. Wasselin, A. Jeantet, and U. Meier, 2008: Wake vortex profiling by doppler X-band radar: Orly trials at initial take-off & ILS interception critical areas. *Proc. IEEE Radar Conference*, IEEE, doi:10.1109/RADAR.2008.4721113.
- Barbagallo, J., 2014: Aircraft wake turbulence. Advisory Circular 90-23G, Federal Aviation Administration.
- Batchelor, G., 1967: *An Introduction to Fluid Dynamics*. Cambridge University Press.
- Beard, K., 1976: Terminal velocity and shape of cloud and precipitation drops aloft. *J. Atmos. Sci.*, **33**, 851–864, doi:10.1175/1520-0469(1976)033%3C0851:TVASOC%3E2.0.CO;2.
- Beckmann, P., 1962: Statistical distribution of the amplitude and phase of a multiply scattered field. *J. of Res. of the Nat. Bureau of Standards—D. Radio Propagation*, **66D (3)**, 231–240, doi:10.6028/jres.066D.026.
- Broderick, A., and Coauthors, 2008: Wake turbulence—An obstacle to increased air traffic capacity. Report, National Research Council of the National Academies.

807 Crouch, J., G. Miller, and P. Spalart, 2001a: Active-control system for breakup of airplane trailing
808 vortices. *AIAA J.*, **39** (12), 2374–2381.

809 Crouch, J., G. Miller, and P. Spalart, 2001b: Development of an active system to break up trailing
810 vortices. *Aero Magazine*, (14), 24–31.

811 Doviak, R., and D. Zrnić, 1984: *Doppler Radar and Weather Observations*. Academic Press,
812 Orlando, Florida.

813 Doyle, T., and F. McGee, 1998: Air traffic and operational data on selected U.S. airports with
814 parallel runways. Tech. Rep. CR-1998-207675, NASA.

815 French, M. M., H. B. Bluestein, I. PopStefanija, C. A. Baldi, and R. T. Bluth, 2014: Mobile,
816 phased-array, doppler radar observations of tornadoes at X band. *Mon. Wea. Rev.*, **142**, 1010–
817 1036, doi:10.1175/MWR-D-13-00101.1.

818 Fritz, B., and W. Hoffmann, 2015: Update to the USDA-ARS fixed-wing spray nozzle mod-
819 els. *Trans. Am. Soc. Agri. & Bio. Engineers (ASABE)*, **58** (2), 281–295, doi:10.13031/trans.58.
820 10896.

821 Gilson, W., 1992: Aircraft wake RCS measurement. Project Report AAW-11, MIT Lincoln Labo-
822 ratory, Lexington, Mass.

823 Görsdorf, U., V. Lehmann, M. Bauer-Pfundstein, G. Peters, D. Vavriv, V. Vinogradov, and
824 V. Volkov, 2015: A 35-GHz polarimetric doppler radar for long-term observations of cloud
825 parameters—Description of system and data processing. *J. Atmos. & Oceanic. Tech.*, **32**, 675–
826 690, doi:10.1175/JTECH-D-14-00066.1.

827 Govindaraju, S. P., and P. G. Saffman, 1971: Flow in a turbulent trailing vortex. *Phys. Fluids*,
828 **14** (10), 2074–2080, doi:10.1063/1.1693295.

829 Haller, G., and T. Sapsis, 2008: Where do inertial particles go in fluid flows. *Physica D*, **237**,
830 573–583, doi:10.1016/j.physd.2007.09.027.

831 Hamazu, K., H. Hashiguchi, T. Wakayama, T. Matsuda, R. Doviak, and S. Fukao, 2003: A 35-
832 GHz scanning doppler radar for fog observations. *J. Atmos. Oceanic Tech.*, **20**, 972–986, doi:
833 10.1175/1520-0426(2003)20(972:AGSDRF)2.0.CO;2.

834 Harris, F., 1978: On the use of windows for harmonic analysis with discrete fourier transforms.
835 *Proc. IEEE*, **66**, 55–83.

836 Ishimaru, A., 1978: *Wave Propagation and Scattering in Random Media*, Vol. 1. Academic Press,
837 New York.

838 Keränen, R., and V. Chandrasekhar, 2014: Detection and estimation of radar reflectivity from weak
839 echo of precipitation in dual-polarized weather radars. *J. Atmos. Oceanic Tech.*, **31**, 1677–1693,
840 doi:10.1175/JTECH-D-13-00155.1.

841 Kollias, P., N. Bharadwaj, K. Widener, I. Jo, and K. Johnson, 2014: Scanning ARM cloud radars.
842 Part I: Operational sampling strategies. *J. Atmos. Oceanic Tech.*, **31**, 569–582, doi:10.1175/
843 JTECH-D-13-00044.1.

844 Kollias, P., E. Clothiaux, M. Miller, B. Albrecht, G. Stephens, and T. Ackerman, 2007: Millimeter-
845 wavelength radars. New frontier in atmospheric cloud and precipitation research. *Bull. Am. Met.*
846 *Soc.*, **88** (10), 1608–1624, doi:10.1175/BAMS-88-10-1608.

847 Lefebvre, A., 1989: *Atomization and Sprays*. Hemisphere.

848 Li, J., X. Wang, and T. Wang, 2011: Modeling the dielectric constant distribution of wake vor-
849 tices. *IEEE Trans. Aerospace & Electronic Systems*, **47** (2), 820–830, doi:10.1109/TAES.2011.
850 5751228.

851 Liebe, H., G. Hufford, and T. Manabe, 1991: A model for the complex permittivity of water at
 852 frequencies below 1 THz. *Int. J. Infrared & Millimeter Waves*, **12** (7), 659–675, doi:10.1007/
 853 BF01008897.

854 Liu, Z., N. Jeannin, F. Vincent, and X. Wang, 2013: Modeling the radar signature of rain-
 855 drops in aircraft wake vortices. *J. Atmos. Oceanic Technol.*, **30** (3), 470–484, doi:10.1175/
 856 JTECH-D-11-00220.1.

857 Lorenzetto, G., and A. Lefebvre, 1977: Measurements of drop size on a plain-jet airblast atomizer.
 858 *AIAA J.*, **15** (7), 1006–1010, doi:10.2514/3.60742.

859 Pruppacher, H., and J. Klett, 1997: *Microphysics of clouds and precipitation*. Kluwer, Dordrecht.

860 Radhakrishnan, K., and A. Hindmarsh, 1993: Description and use of LSODE, the Livermore
 861 solver of ordinary differential equations. Reference Publication 1327, NASA.

862 Rayleigh, J., 1945: *Theory of Sound*, Vol. 1. Dover, New York.

863 Sapsis, T., and G. Haller, 2010: Clustering criterion for inertial particles in two-dimensional time-
 864 periodic and three-dimensional steady flows. *Chaos*, **20**, 017 515:1–11, doi:10.1063/1.3272711.

865 Seliga, T., and J. Mead, 2009: Meter-scale observations of aircraft wake vortices in pre-
 866 cipitation using a high resolution solid-state W-band radar. *34th Conf. on Radar Mete-*
 867 *orology*, American Meteorological Society, P10.25, extended abstract available online as
 868 <https://ams.confex.com/ams/pdfpapers/155796.pdf>.

869 Shariff, K., and A. Wray, 2002: Analysis of the radar reflectivity of aircraft vortex wakes. *J. Fluid*
 870 *Mech.*, **463**, 121–161, doi:10.1017/S0022112002008674.

871 Sonntag, D., 1994: Advancements in the field of hygrometry. *Meteorol. Zeitschrift*, **3**, 51–66.

- 872 Spalart, P., 1996: On the motion of laminar wing wakes in a stratified fluid. *J. Fluid Mech.*, doi:
873 10.1146/annurev.fluid.30.1.107.
- 874 Spalart, P., 1998: Airplane trailing vortices. *Ann. Rev. Fluid Mech.*, doi:10.1146/annurev.fluid.30.
875 1.107.
- 876 Varga, C., J. Lasheras, and E. Hopfinger, 2003: Initial breakup of a small-diameter liquid jet by a
877 high-speed gas stream. *J. Fluid Mech.*, **497**, 405–434.
- 878 White, F., 1974: *Viscous Fluid Flow*. McGraw-Hill, New York.
- 879 Widener, K., N. Bharadwaj, and K. Johnson, 2012: Scanning ARM cloud radar (X/Ka/W-SACR).
880 Tech. Rep. DOE/SC-ARM/TR-113, U.S. Dept. of Energy, Office of Science, Office of Biologi-
881 cal and Environmental Research.
- 882 Yuter, S., 2003: Precipitation radar. *Encyclopedia of Atmospheric Sciences*, J. Holton, J. Pyle, and
883 J. Curry, Eds., Academic Press, Amsterdam, 1833–1851.

884	LIST OF TABLES	
885	Table 1.	IFR separation standards (in nautical miles) for arrivals on the same runway
886		(Barbagallo 2014). 47
887	Table 2.	Aerial nozzle parameters for the operating conditions specified. Notes: 1: ‘Str’
888		denotes a straight-stream. 2: Values obtained from B. Fritz’s Excel program.
889		3: See text for how flow-rates were obtained. 48
890	Table 3.	Parameters of a typical heavy aircraft. 49
891	Table 4.	Radar parameters. EEC: Enterprise Electronics Corp; PRF: Pulse repetition
892		frequency. Note 1: nnn is the power in kW (250, 350, 500, or 1000). Note
893		2: The only value provided to us was for MIRA-35. The value for the other
894		radars was assumed to be the same. Note 3: The value for a perfectly matched
895		filter has been assumed for all radars. Note 4: For a rainfall rate of 12.5 mm/hr
896		(medium to heavy rain). Note 5: MIRA-35 has full sensitivity beyond a range
897		of 360 m (Matthias Bauer-Pfundstein, Private communication). 50
898	Table 5.	Yearly-averaged temperature and humidity when IFR conditions prevail at the
899		five busiest US airports. 51
900	Table 6.	A comparison of SNR1 reflectivity obtained from a single range cell by using
901		the four different nozzles listed in Table ???. The cell center is at $(x, y, z) =$
902		$(6 \text{ nm}, -50 \text{ m}, -230 \text{ m})$. The signed values (\pm) indicate values <i>relative</i> to
903		nozzle 1. MIRA-35, $\tau = 0.2 \mu\text{s}$, $\theta_b = 0.52^\circ$ 52

Leader	Follower				
	Super	Heavy	B757	Large	Small
Super	3	6	7	7	8
Heavy	3	4	5	5	6
B757	3	4	4	4	5
Large	3	3	3	3	4
Small	3	3	3	3	3

TABLE 1. IFR separation standards (in nautical miles) for arrivals on the same runway (Barbagallo 2014).

	Nozzle 1	Nozzle 2	Nozzle 3	Nozzle 4
Model	CP-09	CP-09	CP11TT	Davidon-Triset
Pressure (psi)	90	90	90	90
Airspeed (mph)	175	175	175	175
Deflection-plane/body angle	0°	0°	0°	0°
Fan angle	Str. ¹	Str.	Str.	Str.
Orifice Code			20	
Orifice diameter (in)	0.125	0.172	0.105	0.125
$a_{0.5}$ (μm) ^{Note 2}	178.5	146.5	183	239.5
$a_{0.9}$ (μm) ^{Note 2}	315	303	359	463
a_0 of log-normal	99.02	55.83	79.85	108.3
σ of log-normal	0.443	0.567	0.526	0.514
Flow-rate (gpm) ^{Note 3}	3.70	6.49	3.00	3.06
U_{exit} (m s^{-1})	29.5	27.3	33.9	24.4
No. of nozzles per side	1	1	1	1
Gallons per nm (two sides)	2.96	5.19	2.4	2.45

904 TABLE 2. Aerial nozzle parameters for the operating conditions specified. Notes: 1: ‘Str’ denotes a straight-
905 stream. 2: Values obtained from B. Fritz’s Excel program. 3: See text for how flow-rates were obtained.

Parameter	Value
Weight, W	500,000 lb
Wing span, b	60 m
Vortex spacing, b_0	47.9 m
Vortex circulation, Γ	$526 \text{ m}^2 \text{ s}^{-1}$
Approach speed, U_{app}	150 knots

TABLE 3. Parameters of a typical heavy aircraft.

Manufacturer	EEC	EEC	EEC	Metek	ProSensing
Series	DWSR	DWSR	DWSR		
Model	8501S	nnn1C ^{Note 1}	2001X	MIRA-35	W-SACR
Frequency, f (GHz)	3	5.9	9.6	35.1	93.9
Peak power, P_t (kW)	850	250–1000	200	30	1.7
Reflector diameter (m)	4.2	4.2	2.4	1.2,2.0	0.9
$\frac{1}{2}$ -power beam width, θ_b	1.83°	0.95°	0.95°	0.52°,0.31°	0.30°
Antenna gain, G (dB)	39.5	45	45	50.4,53.5	54.5
Pulse width, τ (μ s)	0.4–2	0.2–3	0.2–2	0.1,0.2,0.4	0.05–2
Range resolution, $c\tau/2$ (m)	60–300	30–450	30–300	15,30,60	7.5–300
PRF (kHz)	0.2–2.4	0.2–2.4	0.2–2.4	2.5,5,10	≤ 20
$U_{\max} = c \text{ PRF}/4f$ (m s ⁻¹)	5–60	2.5–31	1.6–19	5.3,11,21	≤ 16
Receiver noise figure (dB)	2.0	2.0	2.0	6.2	6.0
2-way waveguide loss ^{Note 2} (dB)	0.8	0.8	0.8	0.8	0.8
Finite bandwidth loss ^{Note 3} (dB)	1.8	1.8	1.8	1.8	1.8
Rain attenuation ^{Note 4} (dB/km)	0.005	0.03	0.12	2	7
Minimum range (m)	150 ^{Note 5}				

906 TABLE 4. Radar parameters. EEC: Enterprise Electronics Corp; PRF: Pulse repetition frequency. Note 1: nnn
 907 is the power in kW (250, 350, 500, or 1000). Note 2: The only value provided to us was for MIRA-35. The
 908 value for the other radars was assumed to be the same. Note 3: The value for a perfectly matched filter has been
 909 assumed for all radars. Note 4: For a rainfall rate of 12.5 mm/hr (medium to heavy rain). Note 5: MIRA-35 has
 910 full sensitivity beyond a range of 360 m (Matthias Bauer-Pfundstein, Private communication).

Airport	T (C)	RH	% IFR Reports
ATL	12.5	95.5%	5.3%
LAX	15.2	92.7%	3.5%
DFW	9.7	94.5%	1.4%
ORD	5.3	94.2%	3.7%
JFK	12.1	93.9%	4.8%

TABLE 5. Yearly-averaged temperature and humidity when IFR conditions prevail at the five busiest US airports.

Nozzle no.	gpm	SNR1 (dB)	$\zeta_{\text{nozzle}}^< \text{ (dB m}^6 \text{ s}^{-1}\text{)}$	$\zeta_x \text{ (dB m}^5\text{)}$
near vortex at $x = 6 \text{ nm}$				
1	3.70	19.15	-157.4	-178.8
2	6.49	$+1.03$	$+1.0$	$+0.6$
3	3.00	-1.04	-1.2	-1.4
4	3.06	-0.5	-0.3	-1.0

TABLE 6. A comparison of SNR1 reflectivity obtained from a single range cell by using the four different nozzles listed in Table 2. The cell center is at $(x, y, z) = (6 \text{ nm}, -50 \text{ m}, -230 \text{ m})$. The signed values (\pm) indicate values *relative* to nozzle 1. MIRA-35, $\tau = 0.2 \mu\text{s}$, $\theta_b = 0.52^\circ$.

LIST OF FIGURES

Fig. 1.	(a) Probability density function (pdf) of the drop sizes produced by nozzle 1 with the conditions listed in Table ?? . The result is based on parameters provided by B. Fritz's Excel program. (b) Distance required for a droplet of a given size to begin moving with an imposed air flow.	54
Fig. 2.	Back-scattering cross-section σ_b (normalized by the Rayleigh value) and phase-shift ϕ versus droplet radius a at the frequencies considered in this work.	55
Fig. 3.	Temperature and humidity (averaged by month) when IFR conditions prevail at the five busiest U.S. airports	56
Fig. 4.	Simulated SNR1 for five radars in a range-elevation scan of the $x = 6$ nm cross-section behind the aircraft. Panel (a) shows droplets colored by radius in μm . IFR ambient conditions: RH = 92.7%, $T = 15.2$ C. Nozzle 1.	57
Fig. 5.	Simulated SNR1 for W-SACR with a pulse width of $0.05 \mu\text{s}$	58
Fig. 6.	Insensitivity to the initial condition. For panels (a) and (b) droplets were placed randomly on each $1 \text{ m} \times 1 \text{ m}$ square. For (c) and (d) droplets were arranged on a regular grid on each $50 \text{ cm} \times 50 \text{ cm}$ square.	59
Fig. 7.	Gray line: Instantaneous power $P_r(t)$ received from the same range gate due to a sequence of transmitted pulses. The range cell is at $(x, y, z) = (6 \text{ nm}, -50 \text{ m}, -230 \text{ m})$. Green: received powers averaged over segments 512 pulses long. Red: the first term in (??). Panels (a)–(e) are for the same cases as in Figure ??b–f.	60
Fig. 8.	Convergence of pulse statistics when the number of computational droplets is increased by four. The same case as Figure ??d is used (MIRA-35 radar). Note: The solid and dashed lines are nearly coincident.	61
Fig. 9.	SNR1 for a non-IFR condition (RH = 60%, $T = 20$ C). A range elevation scan of the wake cross-section 6 nm behind the aircraft is shown. The white circles in panel (e) are points for which a spectral analysis is presented in Figure ??	62
Fig. 10.	Detection at low SNR1 using spectral processing. Panels (a) and (b) are for the the resolution cell centered on $(x, y, z) = (6 \text{ nm}, -55 \text{ m}, -260 \text{ m})$ which is shown as the white circle to the left in Figure ??e. Panels (c) and (d) are for $(x, y, z) = (6 \text{ nm}, -15 \text{ m}, -255 \text{ m})$ which is shown as the white circle to the right in Figure ??e. The radar is MIRA-35 with $\tau = 0.2 \mu\text{s}$ and PRF = 10 kHz. Non-IFR condition (RH = 60%, $T = 20$ C).	63
Fig. 11.	Power-weighted radial velocity corresponding to Figure ?? . Only points where SNR1 > 1 are colored. The actual radial velocity of the gas is shown in panel (a).	64
Fig. 12.	Decay of tangential velocity due to core diffusion.	65
Fig. 13.	Effect of vortex core diffusion. (a) Droplet configuration. (b) SNR1 in the $x = 6$ nm cross-section. IFR ambient conditions (RH = 92.7%, $T = 15.2$ C). Nozzle 1.	66
Fig. 14.	(a) ζ_x for a droplet trail on one side of the aircraft. “Near the vortex” curves (dashed) were obtained by considering only those droplets that obey $ y < 60 \text{ m}$ and $ z - z_{\text{vort}} < 35 \text{ m}$, z_{vort} being the height of the vortex center. IFR ambient humidity and temperature were assumed.	

953 (b) Droplet size distributions produced by the four nozzles. The solid lines show the exact
 954 log-normal distribution, while the symbols show the distribution for each sample of 27,000
 955 droplets injected into the wake. 67

956 **Fig. 15.** Comparison of three formulas for the drag coefficient of a solid sphere. 68

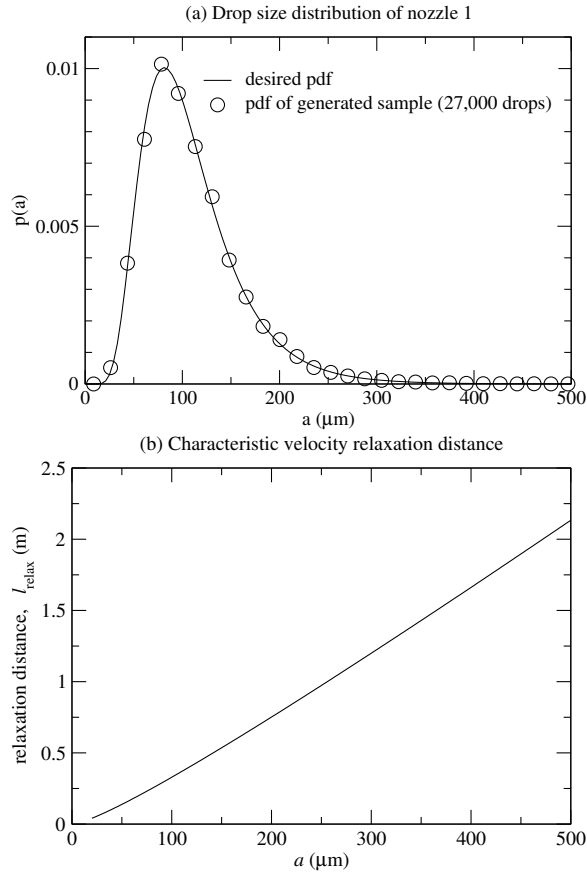


FIG. 1. (a) Probability density function (pdf) of the drop sizes produced by nozzle 1 with the conditions listed in Table 2. The result is based on parameters provided by B. Fritz's Excel program. (b) Distance required for a droplet of a given size to begin moving with an imposed air flow.

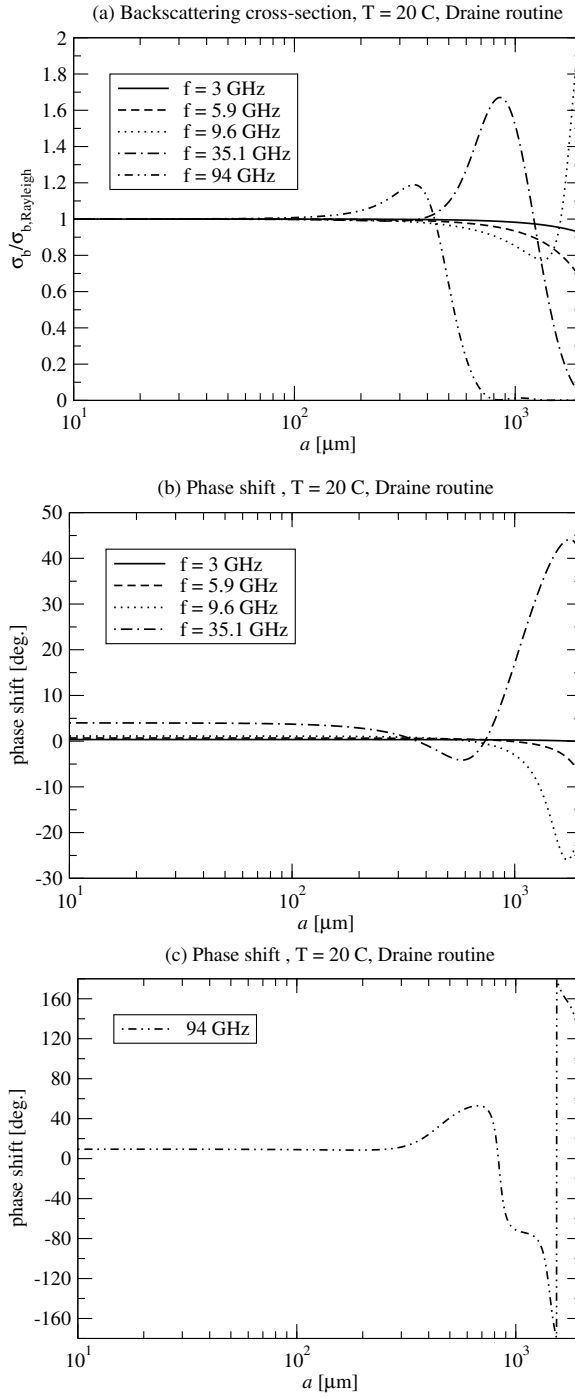


FIG. 2. Back-scattering cross-section σ_b (normalized by the Rayleigh value) and phase-shift ϕ versus droplet radius a at the frequencies considered in this work.

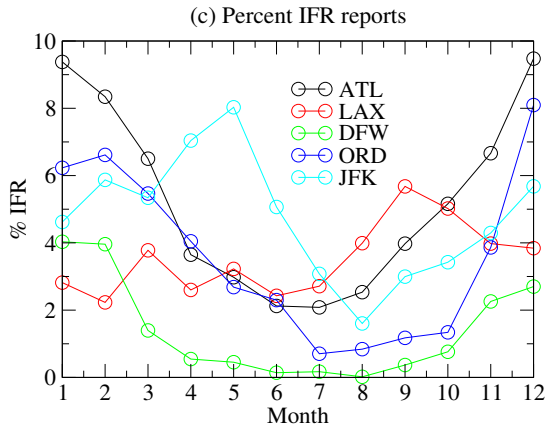
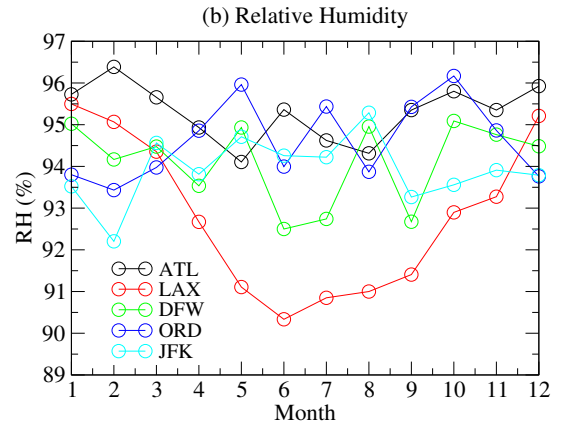
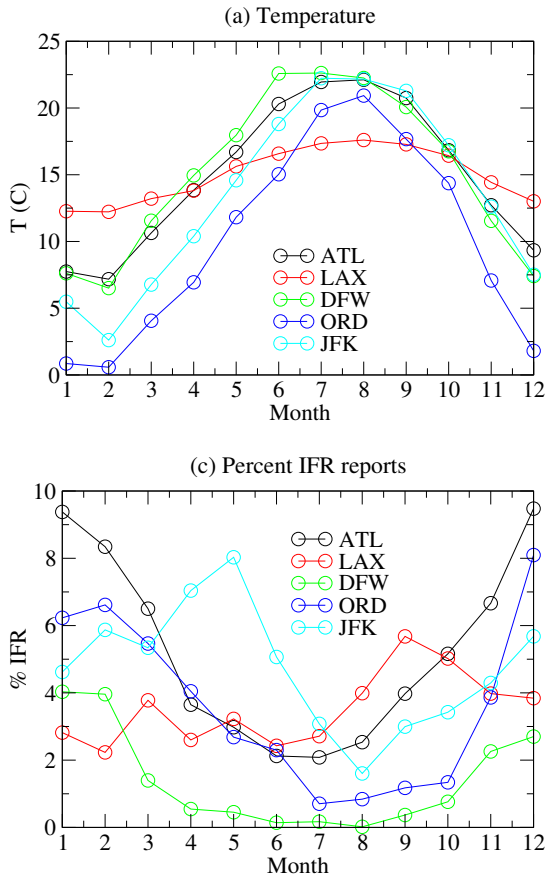


FIG. 3. Temperature and humidity (averaged by month) when IFR conditions prevail at the five busiest U.S.

airports

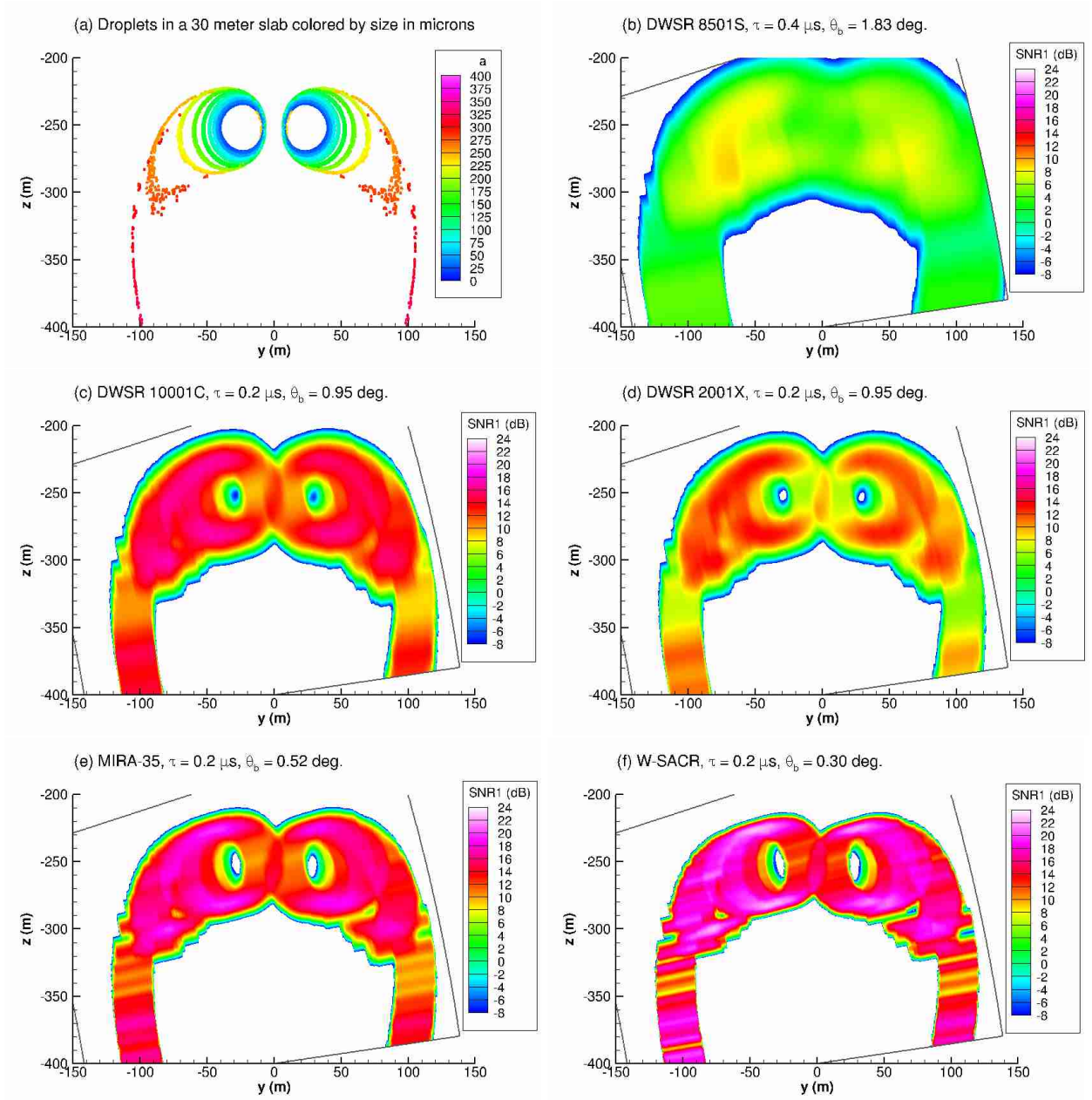


FIG. 4. Simulated SNR1 for five radars in a range-elevation scan of the $x = 6 \text{ nm}$ cross-section behind the aircraft. Panel (a) shows droplets colored by radius in μm . IFR ambient conditions: $\text{RH} = 92.7\%$, $T = 15.2 \text{ C}$. Nozzle 1.

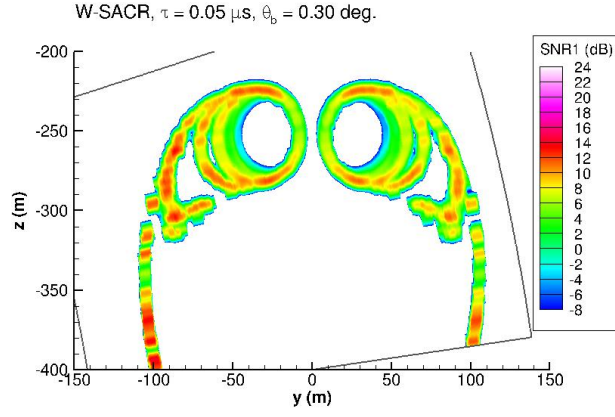


FIG. 5. Simulated SNR1 for W-SACR with a pulse width of $0.05 \mu\text{s}$.

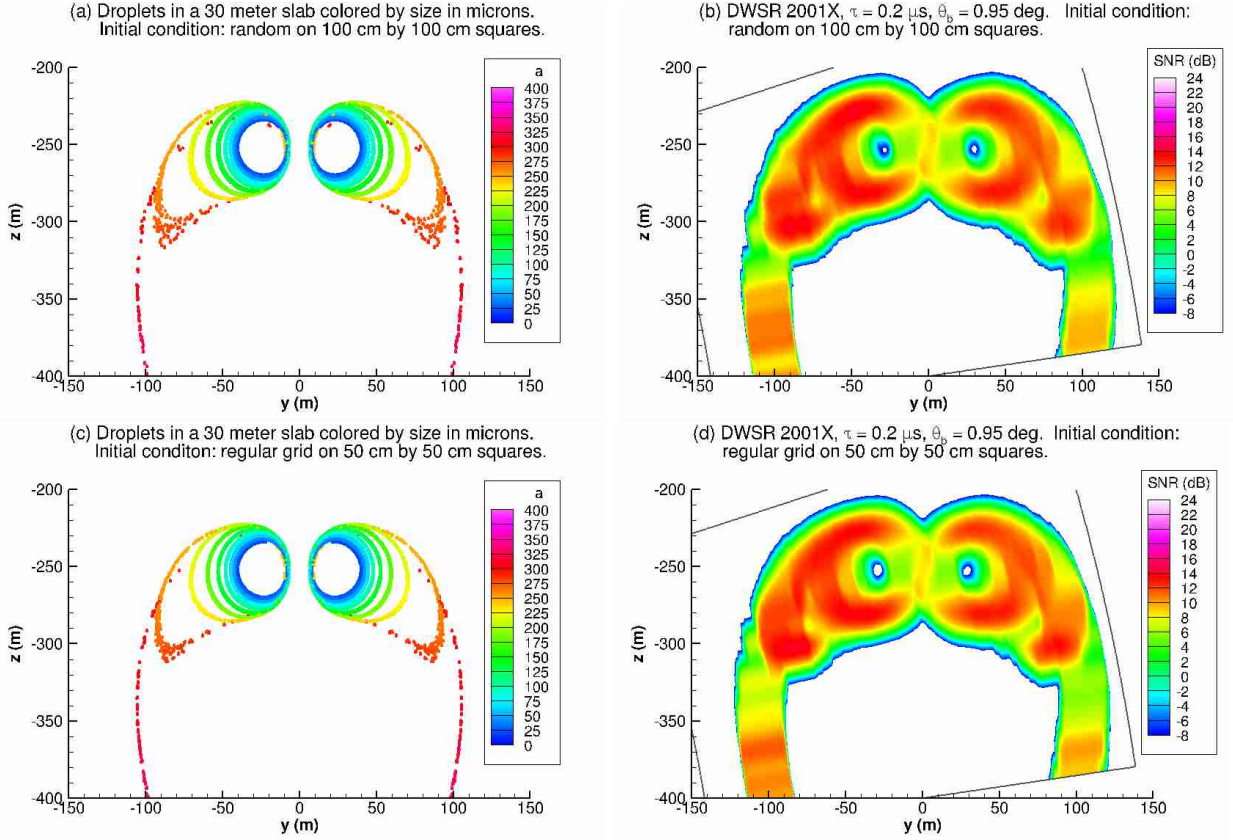


FIG. 6. Insensitivity to the initial condition. For panels (a) and (b) droplets were placed randomly on each $1 \text{ m} \times 1 \text{ m}$ square. For (c) and (d) droplets were arranged on a regular grid on each $50 \text{ cm} \times 50 \text{ cm}$ square.

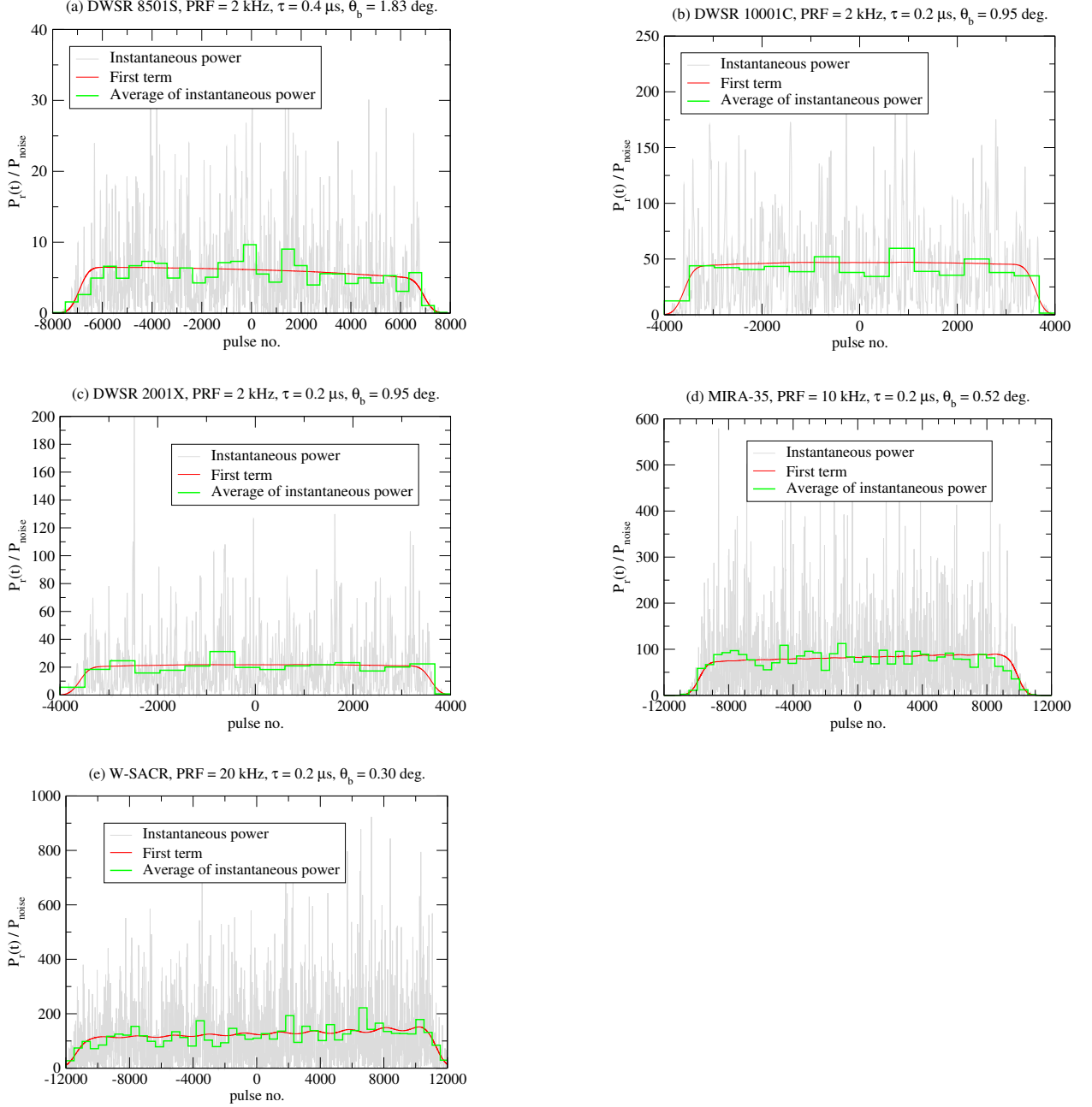


FIG. 7. Gray line: Instantaneous power $P_r(t)$ received from the same range gate due to a sequence of transmitted pulses. The range cell is at $(x, y, z) = (6 \text{ nm}, -50 \text{ m}, -230 \text{ m})$. Green: received powers averaged over segments 512 pulses long. Red: the first term in (23). Panels (a)–(e) are for the same cases as in Figure 4b–f.

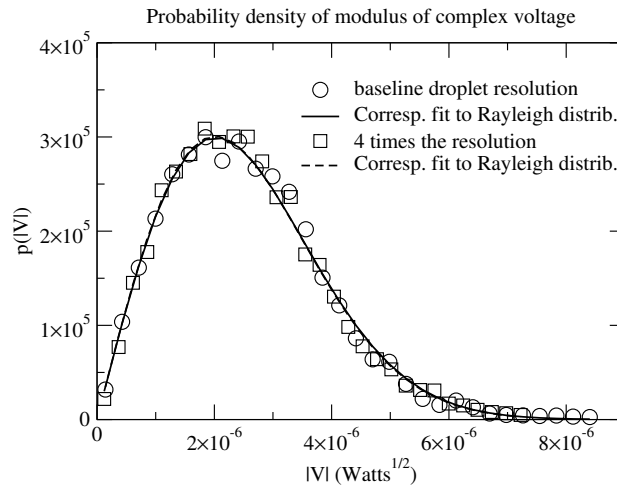


FIG. 8. Convergence of pulse statistics when the number of computational droplets is increased by four. The same case as Figure 7d is used (MIRA-35 radar). Note: The solid and dashed lines are nearly coincident.

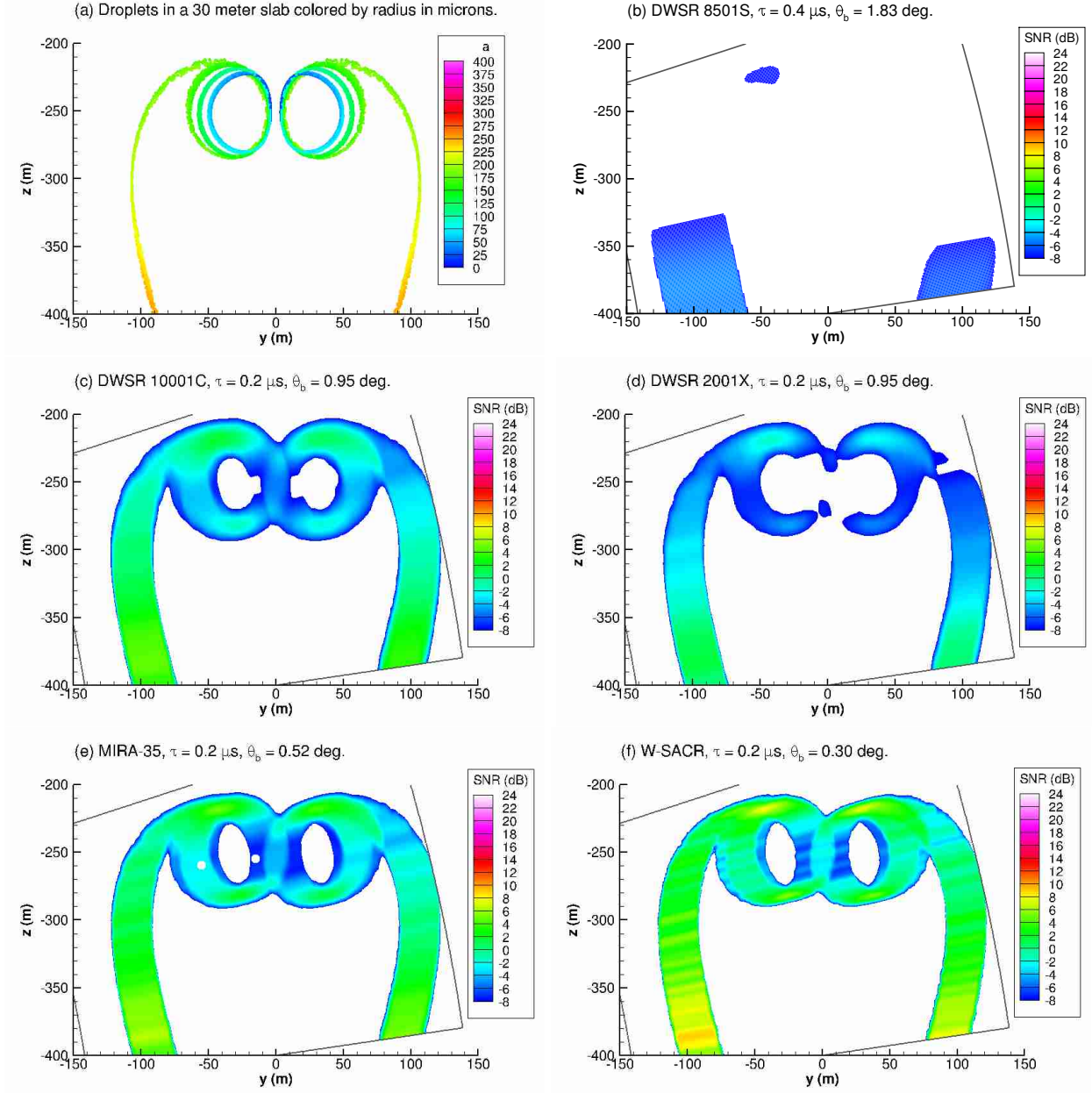
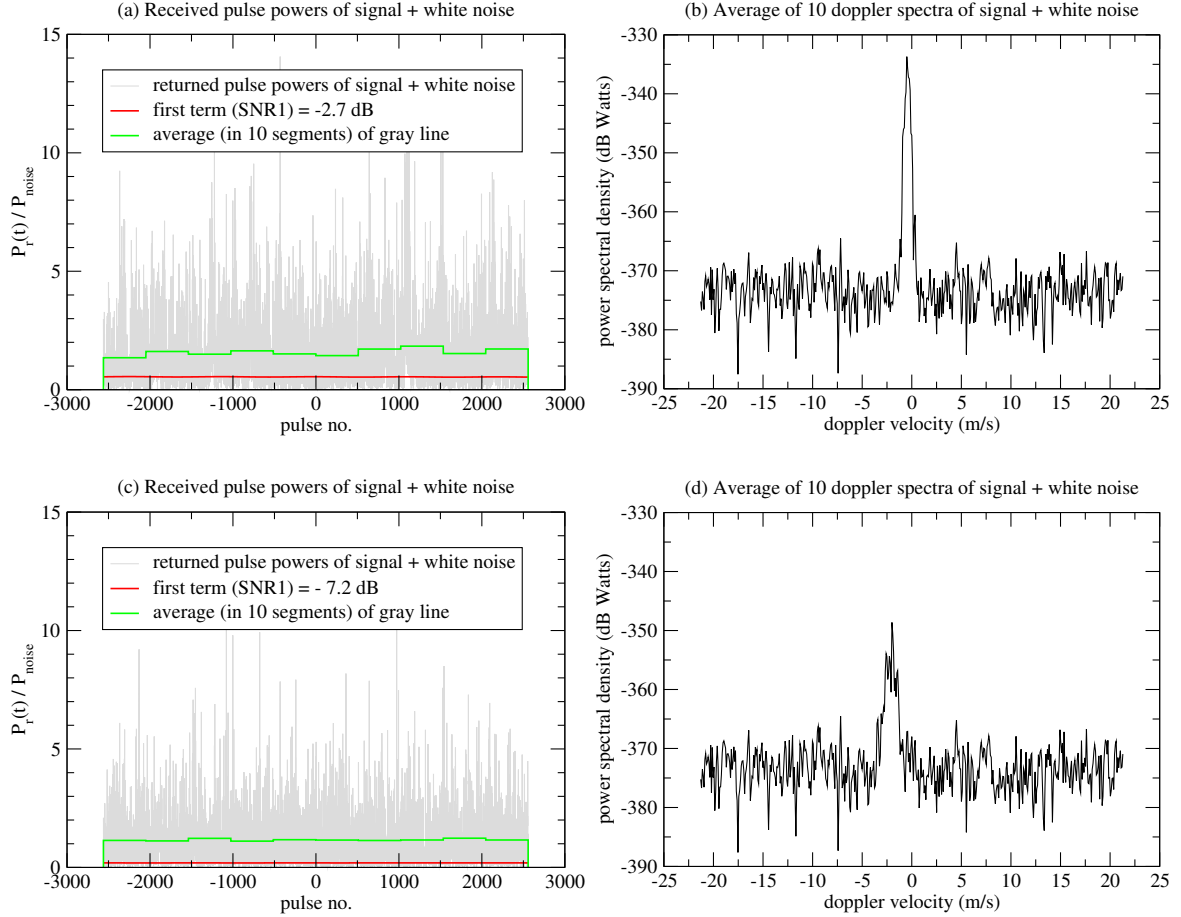


FIG. 9. SNR1 for a non-IFR condition ($\text{RH} = 60\%$, $T = 20 \text{ C}$). A range elevation scan of the wake cross-section 6 nm behind the aircraft is shown. The white circles in panel (e) are points for which a spectral analysis is presented in Figure 10.



977 FIG. 10. Detection at low SNR1 using spectral processing. Panels (a) and (b) are for the the resolution cell
 978 centered on $(x, y, z) = (6 \text{ nm}, -55 \text{ m}, -260 \text{ m})$ which is shown as the white circle to the left in Figure 9e. Panels
 979 (c) and (d) are for $(x, y, z) = (6 \text{ nm}, -15 \text{ m}, -255 \text{ m})$ which is shown as the white circle to the right in Figure 9e.
 980 The radar is MIRA-35 with $\tau = 0.2 \mu\text{s}$ and PRF = 10 kHz. Non-IFR condition (RH = 60%, $T = 20 \text{ C}$).

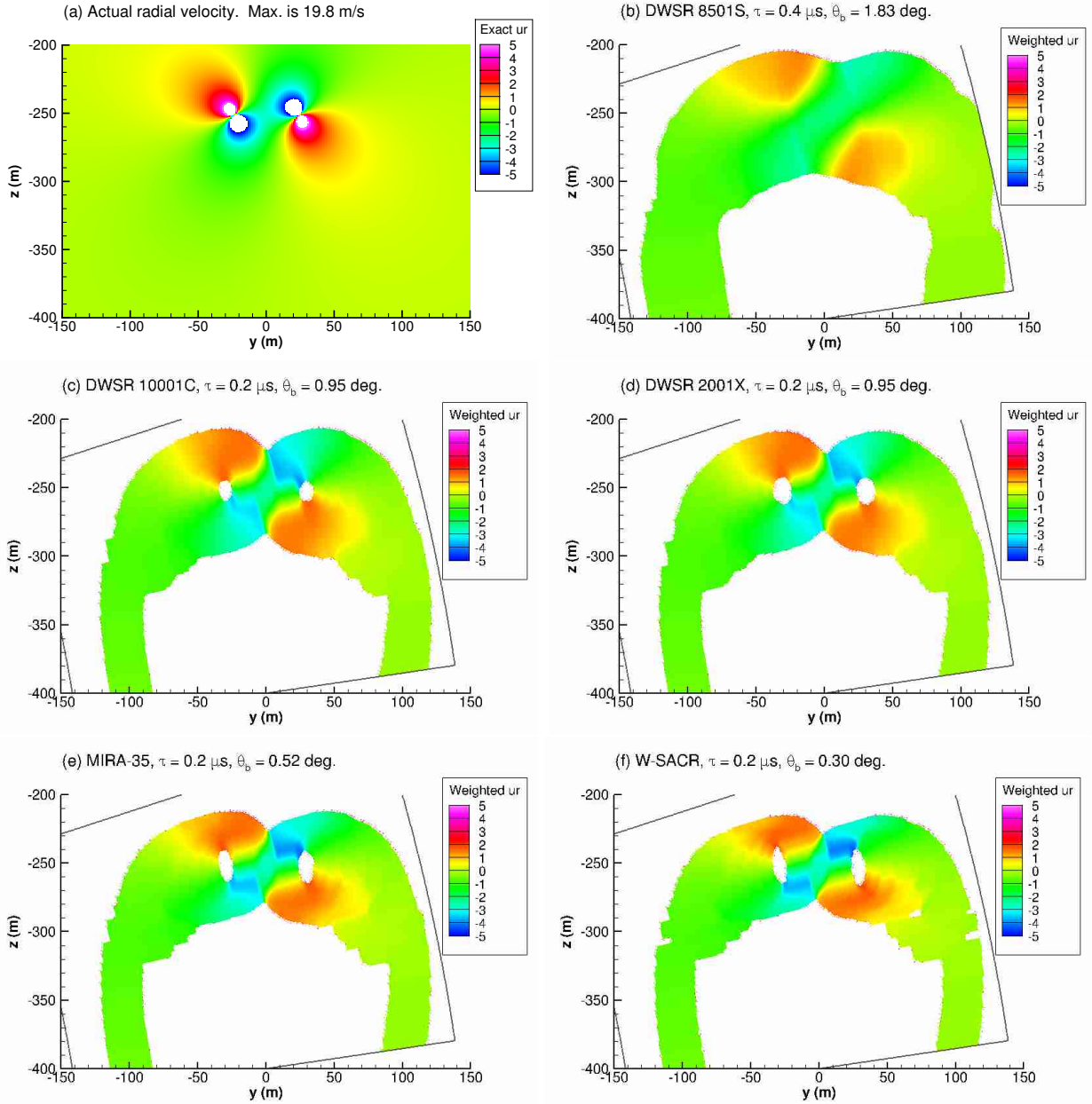


FIG. 11. Power-weighted radial velocity corresponding to Figure 4. Only points where $\text{SNR1} > 1$ are colored.

The actual radial velocity of the gas is shown in panel (a).

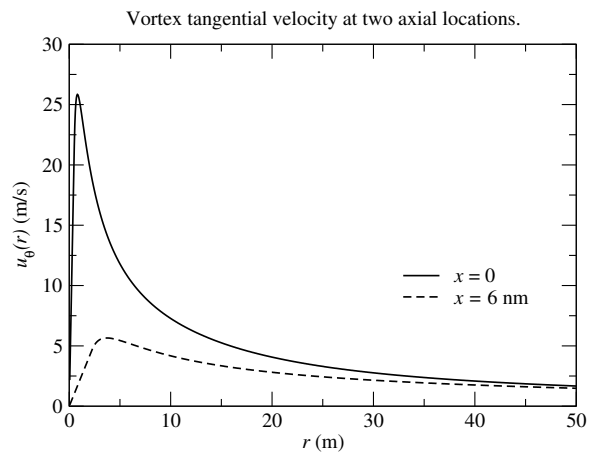


FIG. 12. Decay of tangential velocity due to core diffusion.

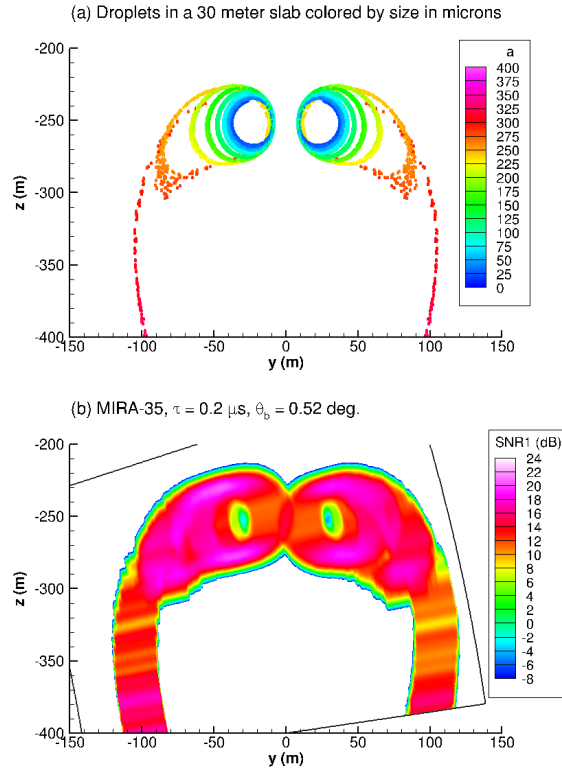


FIG. 13. Effect of vortex core diffusion. (a) Droplet configuration. (b) SNR1 in the $x = 6 \text{ nm}$ cross-section.

IFR ambient conditions ($\text{RH} = 92.7\%$, $T = 15.2 \text{ C}$). Nozzle 1.

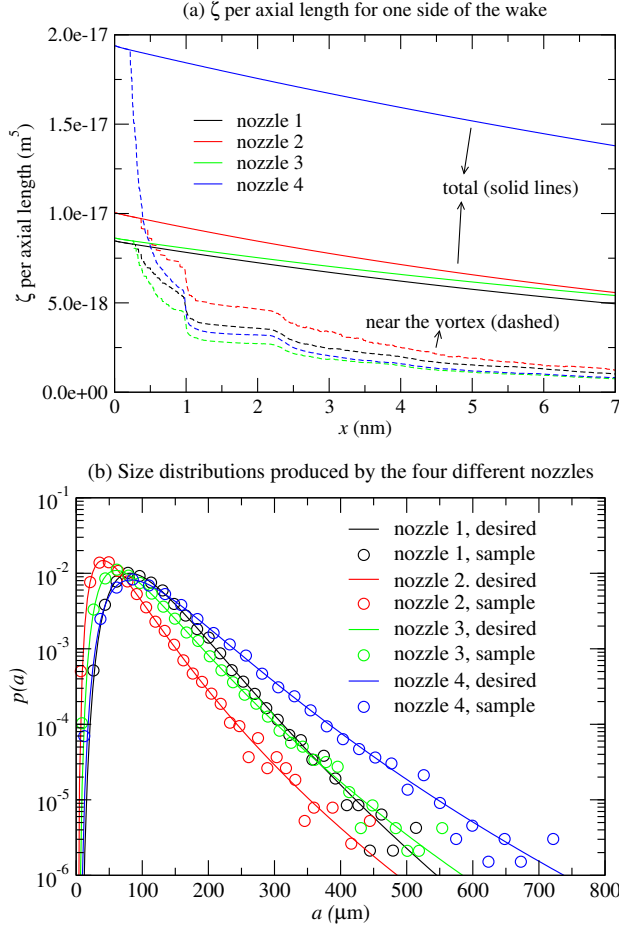


FIG. 14. (a) ζ_x for a droplet trail on one side of the aircraft. “Near the vortex” curves (dashed) were obtained by considering only those droplets that obey $|y| < 60$ m and $|z - z_{\text{vort}}| < 35$ m, z_{vort} being the height of the vortex center. IFR ambient humidity and temperature were assumed. (b) Droplet size distributions produced by the four nozzles. The solid lines show the exact log-normal distribution, while the symbols show the distribution for each sample of 27,000 droplets injected into the wake.

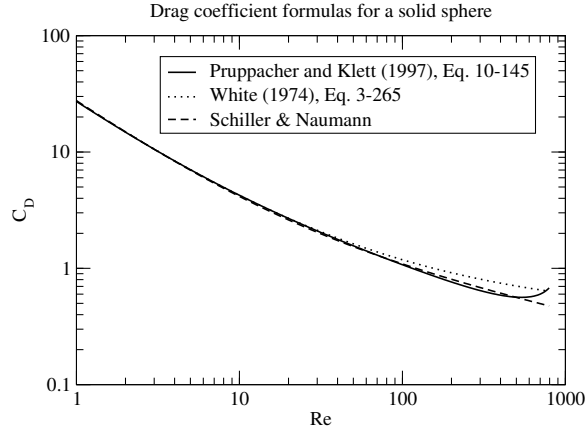


FIG. 15. Comparison of three formulas for the drag coefficient of a solid sphere.